Available online at www.sciencedirect.com
ScienceDirect
Polymer 47 (2006) 6337–6361
polymer
www.elsevier.com/locate/polymer

The effects of processing and organoclay properties on the structure of poly(methyl methacrylate)–clay nanocomposites

Kyle R. Ratinac [a,*], Robert G. Gilbert [b], Lin Ye [c], Allan S. Jones [a], Simon P. Ringer [a]

[a] *Australian Key Centre for Microscopy and Microanalysis (AKCMM), Electron Microscope Unit F09, University of Sydney, Sydney, NSW 2006, Australia*
[b] *Key Centre for Polymer Colloids (KCPC), School of Chemistry F11, University of Sydney, Sydney, NSW 2006, Australia*
[c] *Centre for Advanced Materials Technology (CAMT), School of Aerospace, Mechanical, and Mechatronic Engineering J07, The University of Sydney, Sydney, NSW 2006, Australia*

Received 20 April 2006; received in revised form 26 June 2006; accepted 3 July 2006
Available online 24 July 2006

Abstract

A variety of nanocomposites were synthesised by bulk polymerisation of methyl methacrylate (MMA), and also by extrusion of poly(methyl methacrylate) (PMMA). These were characterised by wide-angle X-ray diffraction (WAXD) and transmission electron microscopy (TEM). We applied image analysis to the TEM images of these PMMA–clay nanocomposites to quantify their structures; an analysis was made of the resulting parameters to determine which were most useful for quantifying the microscale and nanoscale structures. Frequently, these quantitative results differed from those expected on the basis of WAXD, demonstrating the limitations of using diffraction data as the sole measure of nanocomposite structure. By combining the quantitative parameters from TEM with the WAXD data, we have explored the effects of processing conditions and organoclay properties on final nanocomposite structure. Factors examined included the effect of the reactivity of the surface modifiers, platelet size, the incorporation of excess modifier within the organoclay, and bulk polymerisation versus extrusion.

Keywords: PMMA–clay nanocomposites; Electron microscopy; Image analysis

1. Introduction

Polymer–clay nanocomposites (or polymer–layered silicate nanocomposites) comprise dispersions of surface-modified clay platelets – which have a layer thickness under 1 nm – throughout a polymer matrix. Although dependent on the synthetic method used, the essence of forming such nanocomposites is to uniformly disperse or exfoliate the individual platelets throughout the polymer. For example, an organically modified clay (organoclay) may be dispersed into a monomer to form a gel; bulk polymerisation then is initiated in such a way that exfoliation occurs, which typically requires intragallery polymerisation [1–3]. Alternatively, the organoclay may be distributed into a molten polymer by means of melt compounding or extrusion, taking advantage of the viscosity of the polymer and the shear imparted by the screws to exfoliate the platelets [4–6]. Other processing methods include solution casting, emulsion polymerisation and melt intercalation [7–13]. When processed correctly, the nanocomposite typically has physical properties significantly better than those of the parent polymer [5,14–19].

Even a cursory glance at the literature reveals that polymer–clay nanocomposites are the focus of strong research interest worldwide for their promise of large improvements in polymer properties at low filler loadings. In spite of this promise, however, the current commercial applications of polymer–clay nanocomposites are limited by the difficulty in achieving the requisite exfoliated structures across all types of polymers and processing methods. This difficulty is due to our incomplete understanding of the complex experimental factors and interactions that control structural development in these types of systems. Recent reviews of the area [20,21]

* Corresponding author. Tel.: +61 2 9351 4513; fax: +61 2 9351 7682.
E-mail address: kyle.ratinac@emu.usyd.edu.au (K.R. Ratinac).

0032-3861/$ - see front matter © 2006 Elsevier Ltd. All rights reserved.
doi:10.1016/j.polymer.2006.07.005

confirm that significant research is still required to understand the development of structure and to explore the structure–property relationships across the range of polymer–clay nanocomposites. Consequently, the acquisition of quantitative information on nanocomposite morphology is one area of particular importance for advancing the fundamental understanding of these systems. Such quantitative structural data provide the basis for developing processing–structure–property relationships.

Despite the importance of structural characterisation approaches such as wide-angle X-ray diffraction (WAXD) [22,23] and small angle scattering techniques [23–27], transmission electron microscopy (TEM) is the only characterisation method that allows direct observation of nanocomposite structure from the microscale to the nanoscale [28]. At present, relatively few workers have acquired detailed numerical data from TEM images of polymer nanocomposites. In compression-moulded nanocomposite samples, Tabtiang et al. [29] have manually counted the frequency of intersection of clay tactoids with a line perpendicular to the platen surfaces. At higher magnifications, Lan et al. [2] and Vaia et al. [30] have calculated interlayer distances in various structures from micrographs of polymer nanocomposites. Kornmann et al. [31] have applied image analysis to such measurements on high-resolution TEM micrographs. They used the grouping and separation of the intensity maxima and minima in line-scans normal to the silicate layers to estimate the interlayer distances within and the separation between the tactoids. Ranade et al. [32] have used a similar process to measure mean layer separations in poly(amide-imide) nanocomposites.

Other workers have done more comprehensive measurements that provide a greater indication of the degree of exfoliation in nanocomposite structures and are more relevant to mechanical modelling. For instance, Nam et al. [33] have obtained, presumably by manual measurement methods, values of mean thickness, length and aspect ratio, as well as correlation length (*i.e.*, separation), of organoclay particles dispersed in maleated-polypropylene. Marchant and Jayaraman [34] used an image analysis package to classify and count particles (approximately 150 per sample over four samples) as single layers, stacks and agglomerates. The estimated volume fraction of single layers was multiplied with their estimated intrinsic viscosity (a linear function of the aspect ratios of the particles) to give a parameter that correlated with the rheological behaviour of the nanocomposites. Fu and Qutubuddin [35] have used image analysis to quantify the mean ''stack'' (tactoid) thickness and aspect ratio, the mean number of layers per particle and the degree of exfoliation in bulk-polymerised polystyrene nanocomposites. Perhaps the most significant contribution to this area to-date is a series of studies on extruded nylon-6–layered silicate nanocomposites in which Paul and co-workers [4,5,14,36] have obtained significant amounts of numerical data from TEM images. The initial work made use of manual counting of individual silicate layers within specific field areas to assess the degree of exfoliation as a function of the residence time distributions and degrees of shear provided by different extruder types and configurations during melt compounding [4]. Subsequent studies advanced the quantification process by combining manual particle identification with computer-aided or automated counting and sizing [5,14]. Chavarria and Paul [36] have improved on the accuracy of this approach by doing the manual particle identification electronically on digital images.

Making use of such approaches, Fornes and Paul [14] have obtained information on particle aspect ratio and number of layers per particle in nylon-6 nanocomposites produced by melt compounding (extrusion). These data, along with appropriate material properties, were used in the Halpin–Tsai and Mori–Tanaka composite equations to model the mechanical and heat distortion behaviour of the polymer nanocomposites. Given the necessary limitations of the experimental methods and assumptions, both models were found to describe the behaviour of the nanocomposites quite well, indicating that it is primarily the high stiffness and aspect ratio of the montmorillonite (MMT) platelets that are responsible for the improved properties of these nanocomposites, rather than changes in polymer structure induced by the presence of the layers. Sheng et al. [18] have also used quantitative information from high-magnification TEM images (presumably obtained by manual measurements) to incorporate into the Mori–Tanaka model and to compare with the results of finite element modelling.

More recently, Vermogen et al. [37] have applied image analysis to the different length-scales of nanocomposite structure in an effort to more comprehensively understand the distribution of particle morphologies within extruded polypropylene–clay samples. This involved manually measuring a range of particle dimensions on agglomerates, on tactoids of various sizes and on individual platelets, according to six-particle (size) classifications. From the resulting relative frequencies of the different particle classes, Vermogen et al. [37] interpreted the effects of different extrusion conditions on final nanocomposite structure.

These various studies have confirmed the value of obtaining quantitative structural data in nanocomposite systems for advancing our understanding of these materials in terms of processing–structure and structure–property effects. The purpose of this paper, therefore, is to further investigate the types of data that can be obtained from image analysis of nanocomposites, based on PMMA, at the microscale and nanoscale. We then use the quantitative morphological information to explore how varying processing conditions and organoclay properties influence structural development in PMMA nanocomposites. Additionally, the quantitative data obtained from these PMMA nanocomposites will provide a known, accurate data set for the development of more-automated image analysis methods, a focus of our ongoing work.

2. Experimental method

2.1. Materials

2.1.1. Chemicals

Basic chemicals were obtained from commercial sources (Aldrich, unless otherwise noted) and were (a) 1-bromohexadecane

(BHD, 97%) and 1-bromotetradecane (BTD, 97%); (b) 2-(dimethylamino)ethyl methacrylate (DAEMA, 98%); (c) hydroquinone (HQ, 99%); (d) hexadecyltrimethylammonium bromide (HTAB, 99%), tetradecyltrimethylammonium bromide (TTAB, 99%) and dodecyltrimethylammonium bromide (DTAB, 99%); (e) dodecylamine (DA, 99+%); (f) [2-(methacryloyloxy)ethyl]trimethylammonium chloride (METAC); (g) methyl methacrylate (MMA, 99%); (h) 1-dodecanethiol (DT, 97%, from Fluka); and (i) *tert*-butyl peroxide (TBP, 98%). With the exception of the MMA, which was passed through an inhibitor removal column (Aldrich) before use, these chemicals were used as received. Reactive (*i.e.*, polymerisable) surfactants were synthesised by a room-temperature variant of the procedure of Zeng and Lee [38], because heating to 60 °C caused gelation of the reaction mixture. A 2:1 molar ratio of DAEMA and BHD (or BTD) was mixed using a magnetic stirrer for 72 h at room temperature in the presence of inhibitor (HQ > 0.3 wt%). The resulting white precipitate was filtered and washed repeatedly with cold ethyl acetate, then dried under vacuum. ^{1}H NMR spectroscopy of the powder dissolved in deuterated chloroform confirmed that the product was [2-(methacryloyloxy)ethyl]-hexadecyldimethylammonium bromide (MEHDAB) (or [2-(methacryloyloxy)ethyl]tetradecyldimethylammonium bromide (METDAB) when BTD was used).

2.1.2. Clays

The organoclays used in this work were derived from two clays: (1) a commercial Wyoming MMT (Cloisite Na, Southern Clay Products, Inc.) [39] and (2) a commercial bentonite (Trubond, Unimin Australia Ltd.). The Wyoming MMT was not used directly in this work, but was already in the form of two commercial organoclays, Cloisite 93A and Cloisite 30B (Southern Clay Products, Inc.; supplied by Jim Chambers & Associates). The properties of the parent Wyoming MMT are summarised in Table 1. The bentonite sample was received as the predominantly Na^+-form of the clay and, as described later, was used to synthesize other organoclays. The as-received bentonite comprised MMT with significant silica contamination; the estimated composition is 62 ± 6 wt% MMT, 28 ± 3 wt% cristobalite, 8 ± 1 wt% quartz, and 2 ± 1 wt% feldspars (from SIROQUANT (Sietronics Pty. Ltd., Australia) quantitative analysis of the X-ray diffraction data in Fig. 1(a)). The properties of various size fractions of the bentonite are summarised in Table 1. From this, it is evident that even the <150 nm equivalent spherical diameter (e.s.d.) size fraction retained a significant impurity level; approximately 10–15 wt% of residual cristobalite (from SIROQUANT analysis of Fig. 1(b)). The inability to completely remove cristobalite contamination from bentonite clays is not uncommon [40–42]; it is due, in this case, to the presence of the cristobalite as nanoparticles. The application of transmission electron microscopy (TEM) to resin sections containing dispersed bentonite revealed occasional large clusters of nanoparticles (such as in Fig. 1(c)) as well as the distinctive layered structures of the MMT platelets and tactoids. Several isolated clusters were characterised by nanoprobe energy dispersive X-ray spectroscopy (spectra not shown) and were found to contain only Si and O, as expected for cristobalite (SiO_2); in contrast, Al, Mg, Si and O were detectable during analysis of large MMT particles. The presence of the cristobalite as nanoparticles accounts for the difficulty in removing this contamination from the MMT. Consequently, it was decided not to attempt to retrieve a highly purified sample of the MMT prior to organoclay synthesis. Instead, the <5 μm fraction (e.s.d.), which from Table 1 is essentially identical to the traditional "clay" fraction of <2 μm (e.s.d.), was selected to provide the largest amount of material for organoclay synthesis without any of the coarse contaminants (predominantly quartz).

It is noteworthy that the CEC estimated from the data of Laird [47] and the measured mean layer charge of the MMT in the bentonite (Table 1) was 0.84 mmol g^{-1}. This theoretical CEC value shows good agreement with the extrapolation of

Table 1
Properties of the two montmorillonitic clays from which all of the organoclays were derived

Clay	Fraction[a]	MMT content[b] (wt%)	CEC[c] (mmol g^{-1})	Mean layer charge ($e^-/O_{20}(OH)_4$ unit)	Surface area per monovalent exchange site[d] (nm^2)	Mass loss for removal of structural water[e] (wt%)
Cloisite Na	Wyoming MMT [39]	–	0.92 [43]	0.69[f]	0.68	6.5 [5]
Bentonite	As received	62 ± 6	0.663 ± 0.002	0.62 ± 0.08[g]	0.75 ± 0.11	4.14 ± 0.01
	<5 μm (e.s.d.)	70 ± 6	0.699 ± 0.004			4.78 ± 0.01
	<2 μm (e.s.d.)	70 ± 5	0.697 ± 0.003			Not determined
	<150 nm (e.s.d.)	88 ± 3	0.808 ± 0.006			Not determined
	Extrapolation to 100% MMT	100	0.87 ± 0.05			Not determined

[a] "e.s.d." = equivalent spherical diameter.
[b] Estimated from XRD data with the SIROQUANT program (Sietronics Pty. Ltd., Australia), after baseline subtraction and correction for low-angle intensity aberration. Allowance also was made for orientation of the MMT and quartz phases.
[c] Unless referenced, determined from the photometric method of Meier and Kahr [44] with three replicates per sample.
[d] Calculated from the mean layer charge and surface area per unit cell ($O_{20}(OH)_4$ unit) of 0.933 ± 0.002 nm^2 [11,45,46].
[e] Unless referenced, measured by thermogravimetric analysis (TGA) with a Hi-Res TGA 2950 (TA Instruments, Delaware, USA) as the mass lost over the temperature range 150–1000 °C.
[f] Estimated from interpolation of the CEC versus layer charge data of Laird [47] for eight fully expandable smectites.
[g] Measured by means of the empirical method of Olis et al. [48], with protonated DA as the exchange cation. The large error in this data comes from the standard error in the regression fit of Olis et al. [36]; the reproducibility of the repeat measurements was far better than this value.

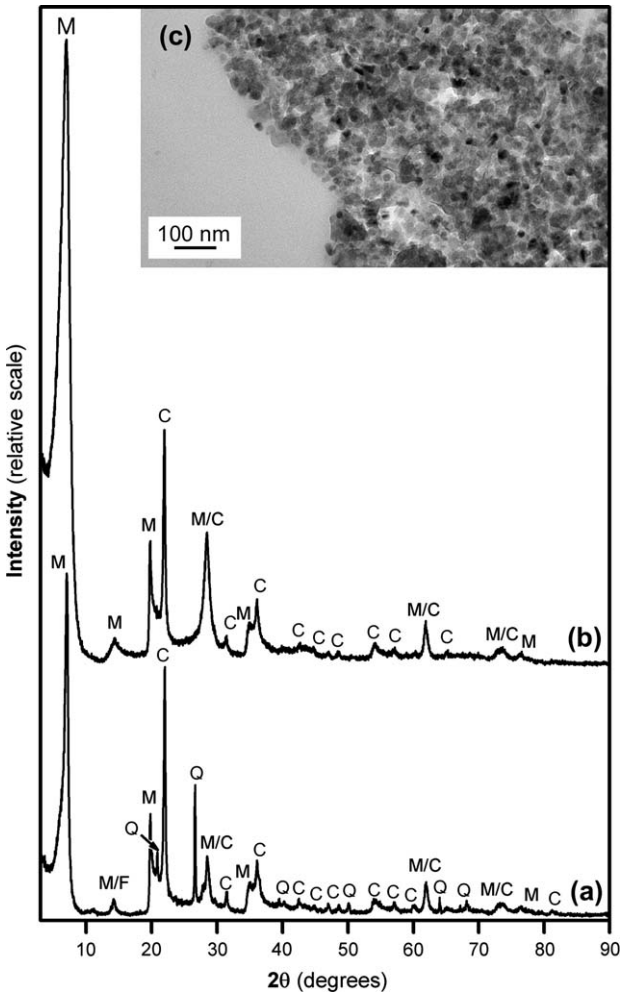

Fig. 1. XRD scans of (a) the as-received bentonite and (b) the <150 nm fraction, where M = montmorillonite, C = cristobalite, Q = quartz, and F = feldspar. Inset (c): TEM image of a cluster of cristobalite nanoparticles in a resin section.

the measured CEC values to 0.87 ± 0.05 mmol g^{-1} at 100% MMT (Table 1), suggesting that the measured compositions and CECs of the various bentonite fractions are accurate. Therefore, the measured CEC of the <5 μm fraction (Table 1) was used to calculate the modifier contents of the organoclays presented below.

2.1.3. Organoclays

The commercial organoclays, Cloisite 93A and Cloisite 30B, were used as received. Cloisite 93A is MMT modified with methyl dehydrogenated-tallow ammonium (MDHTA) ions; Cloisite 30B is MMT modified with bis-2-hydroxyethyl methyl tallow ammonium ($(HE)_2MTA$) ions.

For synthesis of the other organoclays, 1.5 wt% of bentonite was dispersed into Milli-Q water and allowed to settle, leaving only the <5 μm fraction (e.s.d.) in suspension. After decanting, this suspension was cation exchanged according to the method of Zeng and Lee [3]; the molar ratio of surfactant to clay exchange sites, of up to 2.5, was based on the initial mass of bentonite. By washing the exchanged organoclays different number of times with Milli-Q water and/or absolute ethanol, the amounts of excess organic salt retained in the organoclays were varied. After washing, the organoclays made with conventional modifiers (HTAB, TTAB, DTAB) were air-dried at 60 °C for 24 h; those made with reactive modifiers (MEHDAB, METDAB, METAC) were vacuum dried at room temperature for 24 h. The dry organoclays were crushed with a mortar and pestle to pass a 125 μm screen. Selected properties of the organoclays are summarised in Table 2, demonstrating that washing with ethanol removes all the excess organic salt and produces essentially stoichiometric organoclays (91–103% of the CEC). Table 2 also shows the appearance of multiple basal peaks in the organoclays containing excess organic salt, which commonly are observed for such organoclays [49,50], due to the formation of multiple packing configurations of the organic modifiers in the galleries. The measured organic contents of the two commercial organoclays show reasonable agreement with the ''loss on ignition'' or ''organic content'' values presented elsewhere [43,51,52], when allowance is made for loss of structural water by the MMT (as described in Refs. [5,53,54]); this gives 26.7 wt% for Cloisite 30B and 34.1 wt% for Cloisite 93A.

2.2. Synthesis of nanocomposites

The first step in sample formulation was the addition to MMA of 0.2 wt% TBP, as thermal initiator, and 0.7 wt% 1-dodecanethiol (DT), as chain transfer agent. Then known masses (nominally 10 g) of this mixture were distributed among preweighed scintillation vials. Organoclay at 5 wt% solids was added to each vial; these were sealed and sonicated in an ultrasonic bath (Cole Parmer 8891) to homogenise the samples. The bath was filled with an ice–water mixture, replaced as necessary; the standard sonication time was 5 h, which is consistent with typical sonication times used in the literature [1,3,35,67]. The samples then were polymerised in an oven by gradual heating to 90 °C – with a 48 h hold at this temperature – before natural cooling. The scintillation vials were broken to remove the polymerised samples. A total of 17 samples were made in this way, 4 of which were replicates of randomly selected samples.

For comparison with these shear-free bulk-polymerisation conditions, two additional samples were synthesised by shear-intensive melt compounding (extrusion). The samples were extruded from a ZSK-30 intermeshing, co-rotating, twin-screw extruder ($L/D = 30$, $L = 880$ mm; Werner and Pfleiderer, Ramsey, New Jersey). The screw speed was 250 rpm and the temperature profile was decreased along the barrel, feed-end to die-end, from 220 to 190 °C. Oven-dried, pelletised PMMA (Plexiglas 7H, $M_w \sim 150$ kDa; Röhm GmbH & Co. KG, Darmstadt, Germany) was screw-fed into the extruder at 5 kg h^{-1}. Approximately one-third of the way down the length of the barrel, organoclay (Cloisite 30B or Cloisite 93A) was screw-fed into a port in the barrel at 0.265 kg h^{-1}, giving an organoclay content of 5 wt%. The screw configuration was selected to give a medium relative degree of shear; the samples were extruded through a 3 mm

Table 2
Organoclay properties determined from TGA and XRD data

Organic modifier	Sample name	Washing method[a]	Organic content[b] (wt%)	Organic content[c] (% of CEC)	Basal peak position(s)[d] (degrees 2θ)	Basal spacing(s)[d] (nm)	Relative basal peak area(s)[d] (%)	Effective mean d_{001}[e] (nm)	Integral ($00l$) series[f]	Interlayer configuration[g]	ΔHLB[h]
None (Na^+)	MMT	None	N/A	N/A	7.01	1.26	100	1.26	No	N/A	N/A
DTAB	D91	EW	12.8 ± 0.1	91 ± 1	5.45	1.62	100	1.62	No	ML−BL	2.5
	D151	WW	21.55 ± 0.08	151 ± 1	2.01, 4.94	4.39, 1.79	3, 97	1.86	No	SELs (+∼BL)	2.2
TTAB	T103	EW	15.94 ± 0.02	103 ± 1	4.91	1.80	100	1.80	Yes	BL	1.6
HTAB	H99	EW	16.6 ± 0.2	99 ± 2	4.85	1.82	100	1.82	Yes	BL	0.6
	H192	WW	30.58 ± 0.04	192 ± 2	1.63, 3.10, 4.66	5.44, 2.85, 1.90	3, 6, 91	2.07	No	SELs (+∼BL)	6.1
	H260	SWR	38.1 ± 0.1	260 ± 3	1.70, 2.30, 2.95, 4.59	5.20, 3.84, 3.00, 1.93	4, 12, 6, 79	2.34	No	SELs (+∼BL)	8.0
METAC	MA81	WW	9.0 ± 0.1	81 ± 1	6.18	1.43	100	1.43	No	ML−BL	6.2
METDAB	MT161	WW	30.5 ± 0.2	161 ± 2	1.75, 3.28, 4.99	5.06, 2.69, 1.77	6, 22, 72	2.18	No	BL + SELs	8.6
MEHDAB	MH95	EW	20.55 ± 0.04	95 ± 1	4.32	2.05	100	2.05	No	BL−PTL	0.9
	MH138	WW-pAg	28.43 ± 0.03	138 ± 1	1.58, 4.16	5.60, 2.13	0.5, 99.5	2.14	No	SELs (+∼PTL)	4.8
	MH151	WW	30.50 ± 0.04	151 ± 1	1.62, 2.24, 2.92, 4.49	5.45, 3.94, 3.02, 1.97	3, 6, 26, 65	2.47	No	SELs (+∼PTL)	5.7
	MH237	SWR	42.0 ± 0.1	237 ± 2	2.28	3.87	100	3.87	Yes	PS	9.0
$(HE)_2MTA$	C30B[i]	As received	25 ± 0.8	101 ± 3	4.93	1.79	100	1.79	Yes	BL	2.9
MDHTA	C93A[i]	As received	33 ± 0.7	103 ± 2	3.73	2.37	100	2.37	No	PTL−PS	8.9

[a] Organoclay washing conditions after cation exchange are EW = ethanol wash until negative $AgNO_3$ test, WW = water wash until negative $AgNO_3$ test, WW-pAg = several water washes past the point of a negative $AgNO_3$ test, and SWR = single water rinse.

[b] Determined from the TGA data with correction for structural water loss by the MMT.

[c] Calculated on the basis that the surface modifiers are cations for exchange up to the CEC of the clay, and salt molecules for adsorption above the CEC.

[d] From X-ray diffractograms, which were analysed as follows (after the basic approach presented by Janeba et al. [55]): (1) smooth data (by FFT or a very low level of Loess smoothing) and subtract the background; (2) apply Cu $K\alpha_2$ strip; (3) multiply data by the Bragg−Brentano intensity calibration for kaolinite (a layered 1:1 aluminosilicate) presented by Matulis and Taylor [56]; (4) divide the intensity data by the Lorentz-polarisation factor [55] and by the structure factor for a single MMT layer from the data given by Vaia and Liu [22], ignoring the relatively limited effects of the surface modifiers in the interlayer, to obtain an estimate of the interference function independent of angular factors [55]; and (5) deconvolute the interference function with PeakFit 4.11.05 (Systat Software, Inc., Richmond, California, USA) to obtain individual peak properties (angular position, FWHM and relative peak areas), as per the concepts of Stanjek and Friedrich [57]. The d_{001} values determined from Bragg's law with $\lambda = 0.15406$ nm (Cu $K\alpha_1$ radiation).

[e] This is the relative-peak-area-weighted-mean of the d_{001} values for each sample. Thus, for an organoclay with three basal peaks, A, B, and C, positioned at d^{A}_{001}, d^{B}_{001}, and d^{C}_{001}, with relative peak areas of A^A, A^B, and A^C, respectively, the effective mean d_{001} value is $[(d^{A}_{001}A^{A}) + (d^{B}_{001}A^{B}) + (d^{C}_{001}A^{C})]$.

[f] Indicates whether diffractograms showed an integral series of ($00l$) reflections from one or more basal peaks; all confirmed series showed peaks from 002 up to at least 006.

[g] Nominal configuration of the surfactant molecules in the interlayers: ML = monolayer, BL = bilayer, PTL = pseudotrimolecular layer, PS = paraffin structure, SELs = salt expanded layers; ML−BL = mixed structure in ML to BL transition region, etc. [49,58−62].

[h] ΔHLB is the absolute difference between the calculated Davies' hydrophile−lipophile balance, HLB_D, of the surface modifiers and the optimal (or required) HLB of the MMA−clay system, HLB_O [63]. In principle, the smaller the ΔHLB, the more compatible the organoclay−monomer system should be. HLB_O is 20.8 for MMA−MMT [63]. For fully ionised modifiers (*i.e.*, up to stoichiometric exchange), the HLB_D values are simply calculated from the various group contributions presented by Ho [64,65]. For the organoclays containing entrained (*i.e.*, excess) organic salt molecules, the HLB_D values of the salt molecules have been calculated by assuming that − because the salt molecules are neutral in terms of net electrical charge − the group contribution for the anion-neutralised quaternary ammonium head of each salt molecule may be approximated by that of an uncharged tertiary amine. (This assumption implies that the salt molecules are more organophilic than their corresponding cations, in accord with the available experimental information on the relative hydrophobicity of the interlayer environment of organoclays in the presence of excess organic salt [66].) The overall HLB_D value is calculated as the weighted average of the respective HLB_D values from the amounts of cations and salt in the organoclay.

[i] C in the organoclay name stands for "Cloisite".

circular die and water-cooled. Combining the bulk polymerised and extruded samples, therefore, gave a total of 19 samples available for analysis: 15 different sample types and 4 replicates.

2.3. Characterisation techniques

X-ray diffraction (XRD) analyses were done on a Siemens D5000 diffractometer (Siemens Pty. Ltd., Germany). Cu Kα X-rays were generated at 40 mA and 40 kV, and the angular (2θ) scanning rate and step size were $0.08^\circ\,\mathrm{min}^{-1}$ and 0.02°, respectively. For normal XRD, samples were run over a 2θ range of 1–90°; this was reduced to 1–15° (2θ) for wide-angle X-ray diffraction (WAXD). Powder samples (MMT and organoclays) were pressed into a standard cylindrical holder for measurement. Nanocomposite samples (of standard diameter determined by the scintillation vials) were cut at a random height (within an upper height restriction for the diffractometer) and polished to 1 μm surface finish for WAXD analysis.

The organic contents of the organoclays were measured by TGA on a TA Instruments Hi-Res TGA 2950 (TA Instruments, Delaware, USA). Samples were run in high-resolution mode (resolution 5, sensitivity 1, initial heating rate of $50\,^\circ\mathrm{C\,min}^{-1}$) up to 1000 °C in an O_2 atmosphere. The organic content was calculated as the difference between the mass lost by the organoclay and the mass lost by the <5 μm bentonite fraction – to allow for the loss of structural water – over the temperature range 150–1000 °C. Two or three replicates were made for each sample by this method. The results of this technique were confirmed on organoclays by a more labour-intensive depletion method, where the concentration of surfactant remaining in solution after exchange and quantitative washing was determined by HPLC (results not included here). In all cases, the organic contents determined by these two techniques agreed to better than 5% of each other.

To provide some estimate of the compatibility of the organoclays with the MMA, gel volumes were determined (see, for example, [68]). Flat-bottomed, cylindrical glass vials were filled with MMA containing 0.7 wt% DT, to match the polymerisation mixtures as closely as possible, and a 1 wt% loading of organoclay. These were sealed and then sonicated, again in ice water, for 1.5 h, after which the gels were allowed to settle in a vibration-free environment. The final heights of the gel–supernatant interfaces were measured after 48 h; replicate samples showed that reproducibility was within ±2% of the total range.

Polymer nanocomposite samples were prepared for TEM by microtoming. Blocks of suitable dimensions for a microtome chuck were cut at random orientations from the large samples; the melt-compounded samples were prepared for sectioning normal to the direction of extrusion. The blocks were faced-up on a Leica Ultracut S microtome with a glass knife and trimmed to shape with a razor blade. Approximately 0.5 mm square sections were cut from the blocks with a Diatome diamond knife; the nominal thickness of each section was 70 nm. These sections, which were floated on Milli-Q water, were picked up on 200-mesh Cu grids, placed on filter paper, and dried. The dry grids were carbon coated to increase the durability of the sections under the electron beam. TEM characterisation was done with a Philips CM12, operating at an accelerating voltage of 120 kV.

Preliminary TEM characterisation of these samples revealed that image analysis would be necessary at both low and high magnifications to take account of the sample structure at the micrometre and nanometre length-scales. Morgan and Gilman [28], Zeng and Lee [3] and Chen and Tolle [69], among others, have noted that different levels of structure exist in polymer–clay nanocomposites. Magnifications of 7100 times and 110,000 times were considered to provide suitable information at these two length-scales. After the method of Morgan and Gilman [28] and in an effort to obtain representative data, images were taken randomly across two or three Cu TEM specimen grids from at least three sections per grid for each sample. At both magnifications, 15 or more digital images were taken in this manner for each sample to give a reasonably large sample set for statistical analysis of the data. Images were captured at the maximum resolution of a Gatan Multiscan 791 digital camera (1024 × 1024 pixels) running on Gatan Digital Micrograph 2.5.

It was decided that baseline quantitative data on the degree of exfoliation in the samples would be determined from the high-magnification images (110,000 times), because the visibility of the individual platelets at this magnification – whether separated or in tactoids– provides direct data on exfoliation. This choice also accords with the use of high-magnification images for structural quantification in other work [4,5,14,18,31,33,34]. To ensure the reliability of the resulting baseline data, computer-aided manual image analysis was done on these samples. This approach was also necessary because of the inability to achieve accurate, automated segmentation and extraction of the desired quantitative information from high-magnification images [14].

The properties of the particles in each field were determined with the software analySIS Pro 3.2 and 5.0 (Soft Imaging System GmbH, Münster, Germany) as follows. Each field was automatically calibrated to a known spatial standard and a DCE (differential contrast enhancement) filter was applied to increase the ease of detecting platelets. The total number of individual (*i.e.*, exfoliated) silicate platelets was determined manually with the *Touch Count* function. For small, multilayer particles, such as doublets and triplets, the distance across each tactoid, perpendicular to the layers, d_{perp}, was determined with the *Measure Arbitrary Distance* function. These data, combined with the number of layers in each particle, n, allowed calculation of the mean interlayer distance in each particle, d^{T}_{001}, according to $d^{\mathrm{T}}_{001} = d_{\mathrm{perp}}/(n-1)$. For larger particles (*i.e.*, agglomerates), the mean distances perpendicular and parallel to the majority of layers were measured with the *Measure Arbitrary Distance* function. The total number of individual platelets in each agglomerate was also measured with the *Touch Count* function. Pooling the data on single layers and the number of layers in tactoids and agglomerates allowed the distribution of platelet numbers in the particles to be determined for each sample. For each sample, a minimum of 15

fields was analysed in this manner, resulting in total particle counts that varied from 125 up to 1225 per sample, with a mean value of 594. (Alternatively, the total platelet numbers varied from 1559 up to 8018 per sample, with a mean value of 3166.) In addition, estimates of the mean value of and variation in platelet length across the two basic types of parent clays (*i.e.*, bentonite and Cloisite) were made by manual measurement of platelet length with the *Measure Polyline* function. To give confidence of reasonable accuracy, these distances were measured over 15 or 16 fields, randomly selected from all samples containing the same type of parent clay. In this way, 2183 and 1881 platelet lengths were measured across the bentonite and Cloisite samples, respectively.

For the low-magnification images (7100 times), a semi-automated approach was used. This involved automatically calibrating each field to a known spatial standard and application of a background shading correction to remove grey-scale spatial variances associated with acquisition of the TEM images. The optimal threshold for segmentation was then selected manually for each image to allow detection of the clay particles with the automatic *Detect* function. By direct visual comparison of the detected particles with the original image, it was possible to determine where incorrect particle identifications had been made (*i.e.*, where an agglomerate was detected as multiple particles or where separate particles were detected as a single particle). These particles were manually deleted and replaced correctly using the *Delete Particles* and *Append Particles* functions. Once particle identification was finalised, a standard region of interest (ROI) was applied automatically to each image before calculation of the *Particle Results* (not including border particles, *i.e.*, those that crossed the ROI boundary) and two sets of *Frame/ROI Results*, one including border particles one excluding those particles. These latter two data sets were averaged for each field to give ROI results (*i.e.*, number of particles and area fraction of particles in the ROI) representing a count of 50% of the border particles. For each sample, a minimum of 15 fields was analysed in this manner, resulting in total particle counts that varied from 664 up to 20,846 per sample, with a mean value of 9318.

Statistical analysis of the data was done with the software platforms Excel 2003 (Microsoft Corporation, Redmond, WA, USA), JMP 5.1 (SAS Institute, Inc., Cary, NC, USA) and GenStat 7.2 (VSN International Ltd., Hemel Hempstead, UK).

3. Results

For illustrative purposes, two examples of the microstructures and nanostructures obtained in two of the PMMA–clay nanocomposites are shown in Fig. 2. In this work, ''microstructure'' refers to the morphological characteristics on the micrometre scale, such as the number, size, size distribution and spatial distribution of organoclay agglomerates and tactoids. The term ''nanostructure'' describes characteristics on the nanometre scale, such as the number of single platelets, and the number of platelets and their separation within tactoids. The results obtained from the image analysis of these and the other micrographs of all the samples are presented in the following sections.

3.1. High-magnification quantitative data

3.1.1. Distributions of platelet length

The distributions of platelet lengths for the two parent clays used in this work are shown in Fig. 3. These length data were

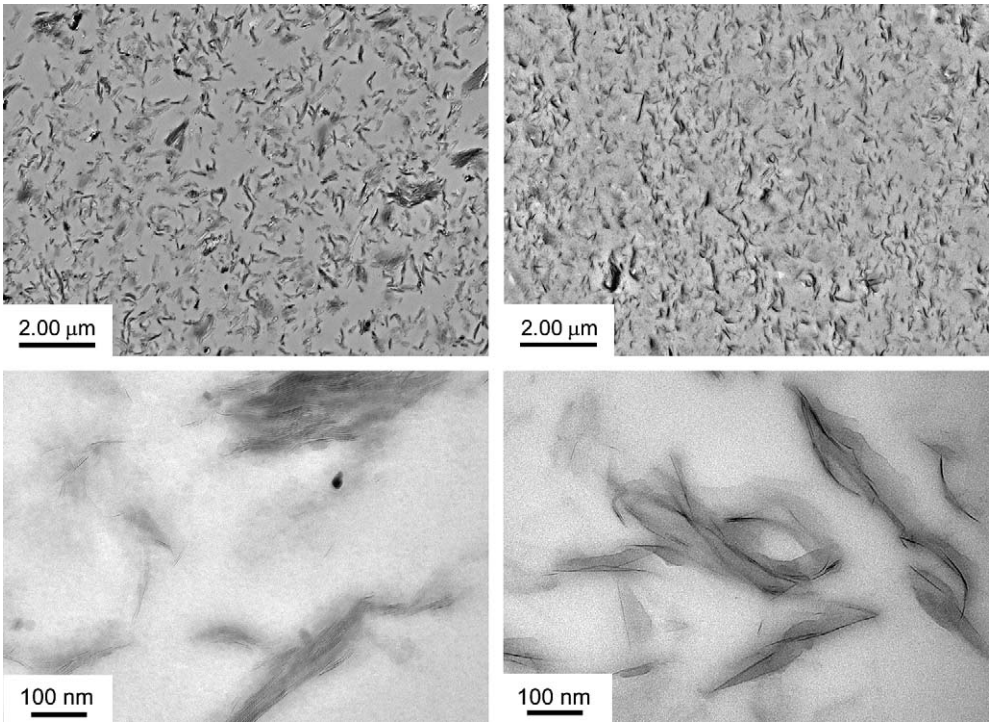

Fig. 2. Two examples of the microstructures and nanostructures obtained in the PMMA–clay nanocomposites.

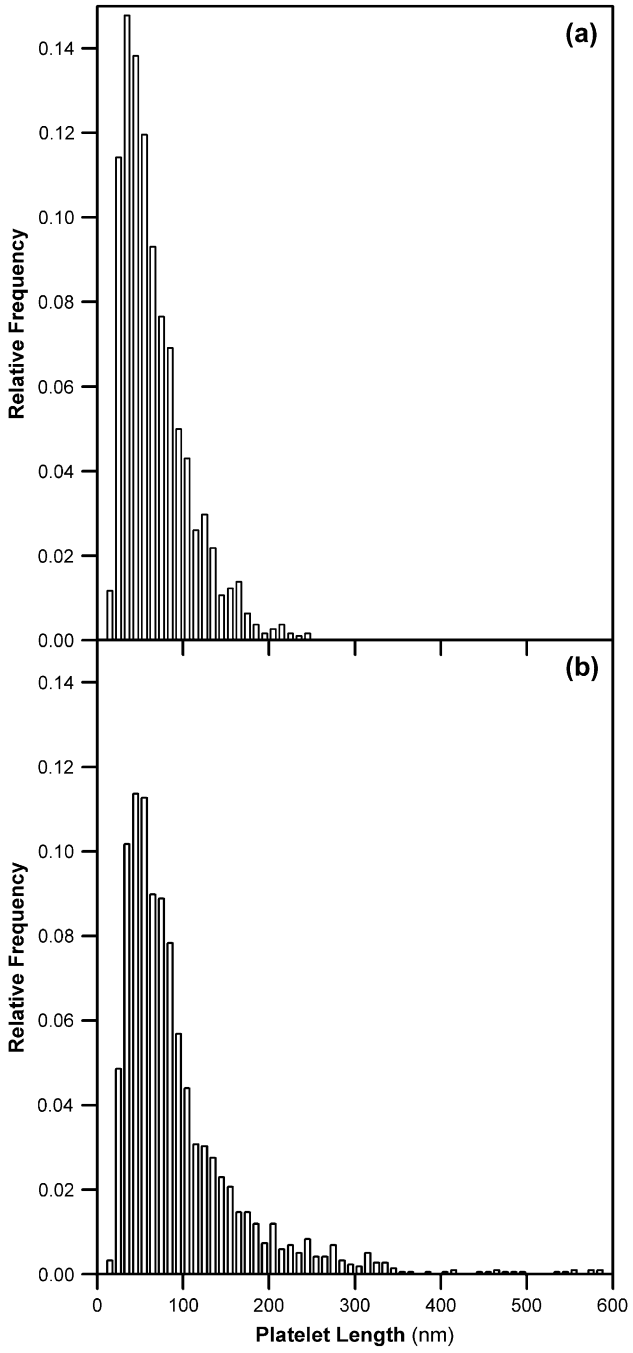

Fig. 3. The frequency distributions of platelet length for the (a) Cloisite and (b) bentonite organoclays used in this work, as measured from nanocomposite samples.

determined by image analysis of platelets dispersed in the PMMA nanocomposites. Both clays display relatively narrow peaks in highly positively skewed distributions, with the bentonite revealing a far longer tail of large platelets (Fig. 3(b)). This tail (maximum of 574 nm) accords with the relatively coarse fractionation of this clay (<5 μm e.s.d.) compared with that expected for the commercial Cloisite clays. This difference also is apparent in the disparity in mean platelet lengths for the two clays: 85 nm for the bentonite and 58 nm for the Cloisite. Nonetheless, these mean values are consistent with the mean platelet length of 70 ± 20 nm determined by Lincoln et al. [26] for a melt-compounded nanocomposite of nylon-6 and Cloisite 30A. Likewise, these values are in line with the mean platelet lengths of between 75 and 82 nm determined for a Cloisite organoclay melt compounded in nylons of medium and high molecular weights [5]. The range of platelet lengths is also consistent with the 50–400 nm diameter tactoids observed by Yaron-Marcovich et al. [70] during TEM characterisation of organoclays. This basic agreement provides support for the accuracy of the platelet-length data collected for bentonite and Cloisite clays used in this work.

3.1.2. Distributions of number of platelets per particle

Consider a typical data set from the high-magnification images. The key parameter measured is the number of platelets per particle, n_i, as determined by analysing (at least) 15 fields with a total area A_f (in μm^2). In this case, i represents the number of particles counted and, therefore, includes all integers from 1 to N_T, where N_T is the total number of particles in the area A_f. If N_n is the number of particles containing n platelets per particle ($N_n \leq N_T$), then the distribution of platelets per particle is obtained by plotting N_n/N_T (*i.e.*, frequency) against n; here n ranges from 1 to j, the largest measured number of platelets per particle. Two of the different distributions thus obtained from the analysis of the high-magnification images are shown in Fig. 4. Despite the large differences in the maximum band values (*i.e.*, largest value of n in the tail) and in the relative frequencies of specific bands, these distributions have similar shapes overall; the maximum frequency occurs at $n = 1$ and rapidly declines as n increases. All 19 samples examined in this work showed this basic sort of distribution shape. Paul and co-workers [14,36,71] also observed similar distribution shapes for extruded nylon nanocomposites containing Cloisite organoclays; in these cases, the distributions were most similar to Fig. 4(b), but with particles only occurring up to $n = 3$ or 4 in nylon-6 and up to $n = 8$ in nylon-66.

The basic similarities of the distribution shapes might be considered suggestive of commonalities in structural development. This is at least partially correct in that the same basic breakdown of the hierarchical MMT particles must occur during the exfoliation process; *i.e.*, from agglomerates to tactoids to single platelets. Because of this hierarchical particle structure, there is a hyperbolic relationship for the total number of platelets, P_n, that are distributed among the N_n particles as n decreases: $N_n = P_n/n$. Although the distribution of P_n as a function of n will vary from sample to sample, this basic hyperbolic relationship probably accounts for some of the similarity in the experimental distributions of N_n/N_T versus n. The other reason for the similarities in the shapes of these distributions is the inverse relationship between field size and the total number of particles that can be observed as n increases. At 110,000 times magnification, the area of a single field is 0.7660 μm^2. Thus, the largest particle that can be seen in a field is one that just occupies this area; from the experimental data, this represents an n value of approximately 700–1000, depending on mean layer separation. Clearly, 15 of such particles is the greatest number that could be visible in 15 fields. In

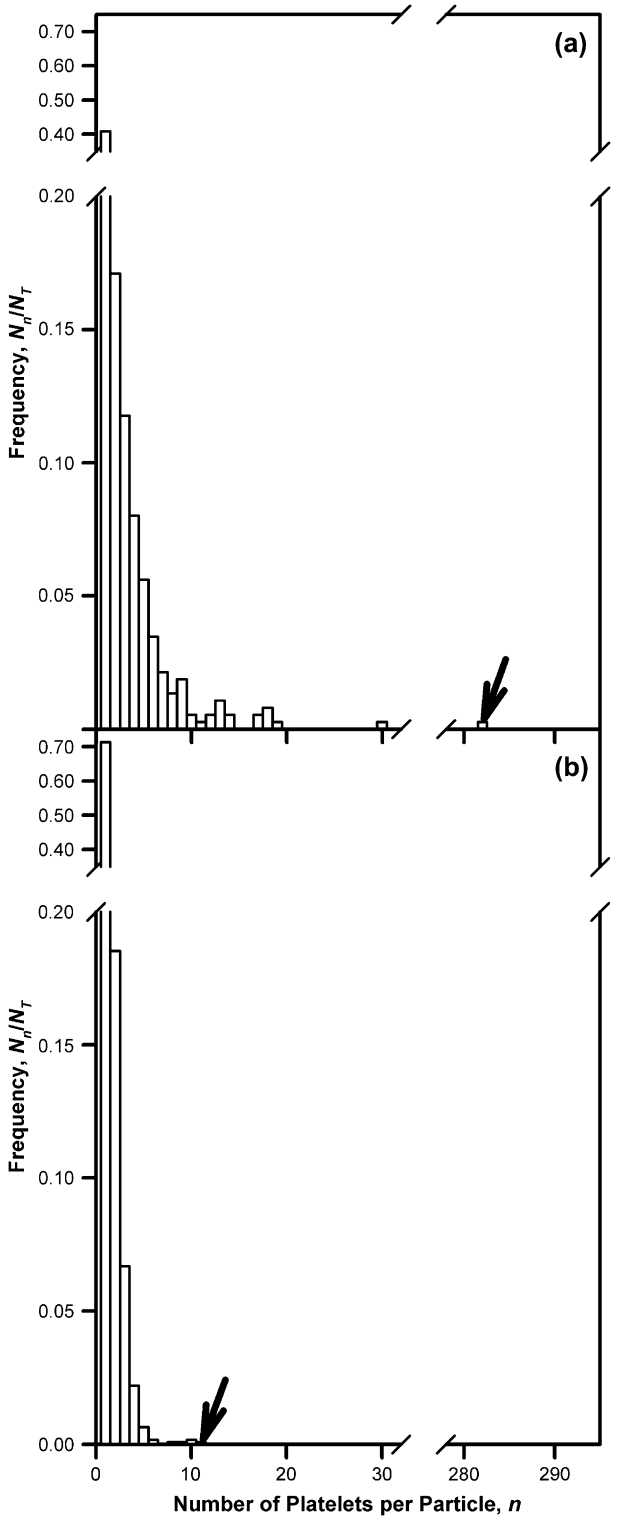

Fig. 4. Two examples of the histograms obtained from image analysis of the high-magnification images of the nanocomposites, in which the maximum band values are marked with arrows. (Note: 10 bands containing data, each of frequency 0.0027, are not shown in (a) due to the break in the abscissa axis.)

direct contrast, the maximum number of exfoliated single layers that could be observed in a single field must be far larger than one; an estimate of this number may be obtained from the size of a typical platelet. Taking a mean platelet length of 80 nm, on the basis of the data presented above, a thickness of 0.95 nm and a separation from other platelets of 15 nm on all sides, the area occupied by a single, rigid platelet is 0.0034 μm^2 (assuming the faces of the platelets lie exactly normal to the section). On this basis, up to 225 single layers could be observed in a single field of area 0.7660 μm^2. Therefore, the possible number of single platelets in one field is more than an order of magnitude larger than that of the large, field-filling agglomerates across 15 fields. Extending these sorts of considerations to intermediate values of n leads to the prediction of the observed distribution shape, where N_n (or N_n/N_T) decreases rapidly with increasing n. Together, these two effects – the hyperbolic relationship between N_n and P_n, and the effect of field size – are responsible for the overall similarities in the shapes of the experimental distributions.

Despite these basic similarities, there are statistically significant differences among many of the distributions, as shown by a series of pair-wise Kolmogorov–Smirnov analyses (see, for example, Ref. [72]) across all the distributions. Of the 171 available pairs of distributions, 92 (or approximately 54%) had P-values of less than 0.05, as determined from the cumulative distribution function given by Smirnov [73]. (In any hypothesis test, the P-value is the smallest level of statistical significance at which the null hypothesis – usually that there is no difference in means – would be rejected. In other words, the P-value is the smallest value of α at which the difference in the data is statistically significant. Thus, smaller P-values indicate more statistically significant differences.) Importantly, all four pairs of replicate samples had P-values greater than 0.85, indicating that the replicate distributions are statistically similar as required to have confidence in sample reproducibility.

3.1.3. Parameters for summarising the distributions and the extent of exfoliation

For practical use of the data obtained from the analysis of the high-magnification images – for example, in comparing the degree of exfoliation of different nanocomposite samples – the distributions discussed above are cumbersome. Instead, it is desirable to find characteristic parameters that summarise the data into single quantities, which are far more amenable to visual and statistical analysis and comparison. A range of such parameters might be used; selected possibilities are defined in Table 3 with the nomenclature used earlier in discussing the properties of a generic distribution. The first three parameters are common statistics; the remainders are parameters derived from the aspects of the distributions that are expected to provide direct measures of the extent of exfoliation or, conversely, agglomeration. Upon consideration, it becomes evident that some of these parameters are inversely related to one or more of the parameters that more directly quantify exfoliation in the sample. This is the case for F_A by its very definition. It is also true for $\overline{n}$ and SE_n, because the lower limit of all distributions in these samples is constant at $n = 1$; thus, increasing the breadth of the distributions, which increases the values of $\overline{n}$ and SE_n, reduces the degree of exfoliation.

Table 3
Definitions, data ranges and errors of selected statistics and exfoliation parameters used to summarise the platelet distributions of the 19 samples

Parameter	Definition	Data range[a]	Error[b]
Maximum value, j	Largest measured number of platelets per particle	11–1062	106
Arithmetic mean, $\overline{n}$	$= \frac{\sum_{i=1}^{N_T} n_i}{N_T} = \frac{\sum_{n=1}^{j} nN_n}{N_T}$	1.5–64.1	0.7
Standard error, SE_n	$\frac{s}{\sqrt{N_T}} = \left[\frac{\sum_{i=1}^{N_T}(n_i-\overline{n})^2}{N_T(N_T-1)}\right]^{0.5}$	0.03–17.0	0.3
Tactoid density,[c,d] ρ_t (μm^{-2})	$= \frac{N_T}{A_f}\frac{1}{M}$	1.2–28.4	0.6
Single platelet density,[d] ρ_s (μm^{-2})	$= \frac{N_1}{A_f}\frac{1}{M}$	0.5–20	1.1
Exfoliation factor,[d] F_E (μm^{-2})	$= \frac{1}{M}\sum_{n=1}^{j}\frac{1}{n}\frac{N_n}{A_f}$	0.6–23.8	0.3
Degree of exfoliation, D_E (%)	$= 100\frac{N_1}{\sum_{n=1}^{j} nN_n} = 100\frac{\rho_s}{\rho_t \overline{n}}$	0.4–49.0	0.4
Agglomeration factor,[d] F_A (μm^{-2})	$= \frac{1}{M}\sum_{n=2}^{j} n\frac{N_n}{A_f} = \rho_t\overline{n} - \rho_s$	21–105	7

Notes: where the notation is as was used earlier in the text, with the addition of standard deviation, s, and MMT content of a nanocomposite sample, M (in wt%).

[a] The minimum and maximum values from among all 19 samples.

[b] The square root of the mean square error of all the replicate measurements.

[c] The term "tactoid density" includes all single platelets, tactoids and agglomerates. It is used to distinguish the areal density of particles at high magnifications from that at low magnifications, which will be termed "particle density."

[d] These parameters are normalised to the MMT content of each nanocomposite sample, M; in the notation of Fornes and co-workers [5,71], therefore, these normalised parameters are "specific" densities or factors.

(The inverse relationship between $\overline{n}$ and D_E also is evident in the second definition of D_E given in Table 3.) Consequently, these three parameters were included in the subsequent analysis in both their original (F_A, $\overline{n}$ and SE_n) and inverted forms (F_A^{-1}, $\overline{n}^{-1}$ and SE_n^{-1}).

The practical value of such parameters depends on how well they (1) characterise the different aspects of nanocomposite structure and (2) allow us to distinguish between structures that actually are significantly different. The first issue depends upon the nature of parameters chosen: for example, F_E amplifies the effects of the smallest particles, particularly the single platelets; in contrast, F_A emphasises the agglomerates in the upper tails of the distributions. The second issue relates to the spread or range of each parameter relative to its reproducibility. In statistical terminology, this is the magnitude of the variance *among samples* relative to the variance *within samples* (*i.e.*, among the replicates). To investigate the latter issue, the "data separation" for each parameter in Table 3 was assessed by means of one-way analysis of variance (ANOVA) and pair-wise comparisons with the Tukey HSD test (or Tukey–Kramer multiple comparisons' test). The results of these tests are summarised in Table 4. The one-way ANOVA indicates the probability of the least one statistically significant difference among the 19 values for each parameter (as quantified in the P-value). It is evident that all parameters have P-values less than 0.05, with most less than 0.0001. Because of the diverse samples (processing conditions) examined here, it is hardly surprising that at least one mean value among the 19 samples for each parameter is significantly different from the grand mean, resulting in these small P-values. Clearly, therefore, ANOVA provides little ability to distinguish the extent of data separation of each parameter.

Table 4
Analysis of "data separation" across the parameters selected to summarise the distributions of number of platelets per particle

Parameter	P-value[a]	Proportion of significant pair-wise differences[b] (%)
j	0.0312	3
F_A	0.0053	17
SE_n	<0.0001	26
$\overline{n}$	<0.0001	42
F_A^{-1}	<0.0001	55
$\overline{n}^{-1}$	<0.0001	71
SE_n^{-1}	<0.0001	76
ρ_t	<0.0001	78
ρ_s	<0.0001	86
F_E	<0.0001	86
D_E	<0.0001	87

Parameters are presented in order of increasing data separation, *i.e.*, by the third column.

Notes: where, as defined in Table 3, j is the maximum value in the distribution, $\overline{n}$ is the arithmetic mean, SE_n is the standard error, ρ_t is the tactoid density, ρ_s is the single platelet density, F_E is the exfoliation factor, D_E is the degree of exfoliation, and F_A is the agglomeration factor. Exponents of "−1" indicate inverse parameters.

[a] From one-way ANOVA; null hypothesis is the difference between all means = 0.

[b] Out of an absolute total of 105 possible pair-wise differences, as tested at $\alpha = 0.05$ with the Tukey–Kramer multiple comparisons' test.

The pair-wise comparisons under the Tukey–Kramer test are more informative, with proportions of significant pair-wise comparisons from 3 to 87%. As outlined earlier, approximately 54% of the pair-wise Kolmogorov–Smirnov analyses among the distributions had P-values less than 0.05; a value of 54% seems, therefore, a natural cut-off point to distinguish between poor and good data separation in Table 4. On that basis, j, F_A, SE_n and $\overline{n}$ all show poor data separation. These are the parameters that either relate directly to or are affected by the large agglomerates in the nanocomposites. Thus, these parameters are sensitive to the large scatter in the properties of the agglomerates – the particles that occur least frequently and are most sensitive to field size effects – which leads to the largest errors across the replicates. For example, the mean ratio of error to data range (from the fourth and third columns of Table 3) for these four parameters is 0.054; by comparison, this mean ratio for the remaining parameters in Table 4 is only 0.017. These remaining parameters all show good data separation; these are the exfoliation and inverted parameters. Evidently, the parameters that quantify or relate to exfoliation provide greatest data separation due to larger differences among the samples and/or improved reproducibility for the replicate samples.

Given that only the exfoliation-related parameters show good data separation, we might anticipate that these

parameters will tend to correlate with one another. This expectation is confirmed by the correlations presented in Table 5; it is clear that these parameters have moderate-to-excellent correlations with D_E. Consequently, for most purposes it will be sufficient to consider only one of these parameters – D_E is the obvious candidate – to characterise the nanostructure of the samples. From this analysis, therefore, we have achieved the goal of finding a suitable parameter to summarise the high-magnification distributions. As further confirmation of the suitability of D_E to describe nanocomposite structure, Fig. 5 presents a visual correlation of sample structure with D_E. Naturally, it can be difficult to visually interpret single, high-magnification images in terms of greater or lesser levels of exfoliation: hence the need for quantitative image analysis. Moreover, many of the single platelets are not visible in these images at the reduced sizes required for publication. Nonetheless, there is an evident trend in Fig. 5 of decreasing tactoid size and generally finer structure with increasing values of D_E.

From Fig. 5 (or the data range in Table 3), it is apparent that D_E varies significantly across the 19 samples examined in this work, reaching a maximum of 49%. For comparison, it is possible to calculate D_E for the various histograms of number of platelets per particle obtained by Paul and co-workers [14,36,71], which were mentioned earlier. The result of these calculations is a range of D_E values between 33 and 56%, with a mean value of 49%. The highest value of D_E obtained in this work approaches the upper values obtained by Paul and co-workers [14,36,71]. Perhaps it is then unsurprising that the two samples with the largest D_E values (49 and 34%) in this work were the extruded PMMA–Cloisite nanocomposites. However, it is noteworthy that, despite achieving similar D_E values, the extruded PMMA nanocomposites have significantly lower ρ_t values than their nylon counterparts. The ρ_t values of the former were 20 and 28 μm^{-2}; in more optimised nylon systems, Paul and co-workers [5,36,71] obtained specific particle densities (approximately equivalent to ρ_t) of 28–135 μm^{-2}, with a mean value of 75 μm^{-2}. Clearly the smaller ρ_t values in this work are consistent with the longer tails in the distributions of N_n/N_T versus n in comparison with the upper limits of $n = 3$, 4 or 8 in the nylon systems of Paul and co-workers [14,36,71]. In future work, it might be possible to further increase exfoliation of extruded PMMA–Cloisite nanocomposites by optimising extrusion conditions as described by Dennis et al. [4].

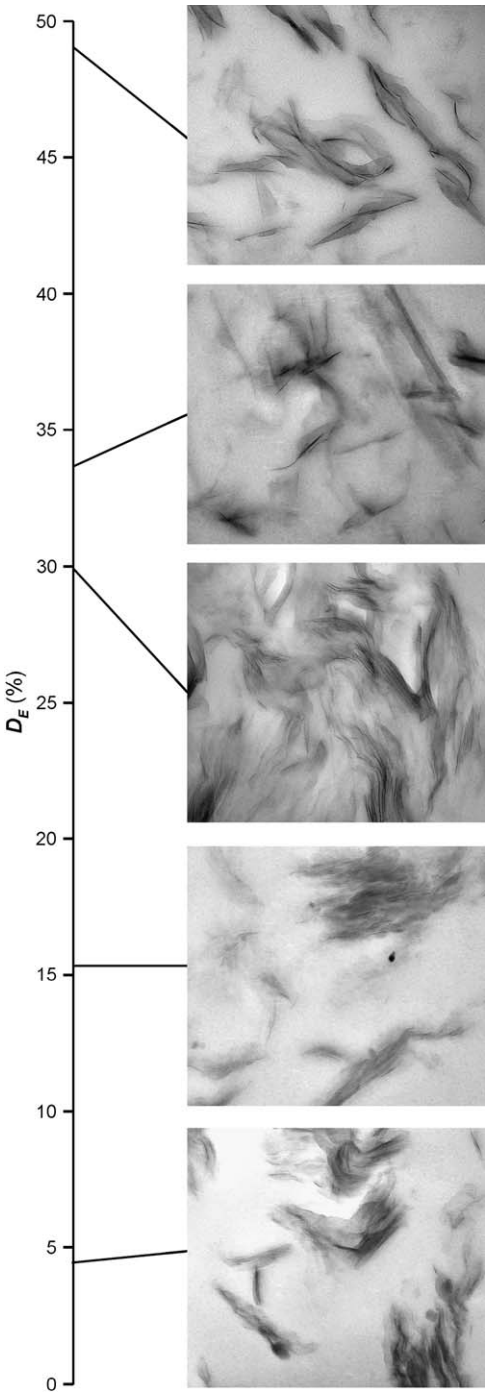

Fig. 5. Visual correlation of sample nanostructure with the degree of exfoliation, D_E. The horizontal length of each field is 875 nm.

Table 5
Correlations between D_E and the other parameters with proportions of significant pair-wise differences exceeding 54% in Table 4

Other parameter	Correlation coefficient, r^2
F_A^{-1}	0.87
$\overline{n}^{-1}$	0.97
SE_n^{-1}	0.67
ρ_t	0.75
ρ_s	0.90
F_E	0.87

3.2. Low-magnification quantitative data

As detailed in Section 2.3, particle identification was applied to the low-magnification images, so that the resulting parameters are either particle properties or field properties. The former quantifies particle characteristics such as size and shape; the latter quantifies the characteristics of the particles within the fields, such as the number or spatial arrangement of particles within each field. A selection of particle

and field parameters is presented in Table 6; these were chosen to give a good coverage of different aspects of structure. Each of these particle and field properties has a distribution of measured values. For example, the number of particles characterised per sample ranged from 664 up to 20,846 and the number of fields from 15 up to 18. Consequently, the question again arises as to which statistic is best to summarise these property distributions into characteristic single values. For the field properties (ϕ_A, r_{NND} and ρ_p), the 15–18 data points available per sample are insufficient to generate accurate distributions and, therefore, the best statistics are simply the arithmetic mean and standard error. However, the large data sets of the particle properties produce quite precise distributions, allowing calculation of a wide range of statistics. These can include measures of central location (*e.g.*, mean, median and mode) and variability, measures of distribution asymmetry (*e.g.*, the higher-order moments), and various percentiles. The possible usefulness of each of these statistics depends on the underlying shapes of the distributions – for an approximately normal distribution, it is appropriate and simplest to use the mean and standard error to summarise the data. As the distribution of the data becomes increasingly skewed, some of the alternative statistics might better capture the key differences among the samples.

Table 6
Definitions, data ranges and errors of particle and field properties selected to summarise the microstructures of the 19 samples

Parameter	Definition	Data range[a]	Error[b]
Area fraction,[c] ϕ_A (%)	The percentage area of particles in a field relative to the entire area of the field	0.7–5.7	0.5
Aspect ratio, r_a	The maximum ratio of height to width of a bounding rectangle for a particle	1.93–2.46	0.05
Next neighbour distance, d_{NN} (μm)	The distance from the centroid of a particle to the centroid of the closest adjacent particle	0.21–0.79	0.01
Next neighbour distance ratio, r_{NND}	Let N_F be the number of particles in a field. Then r_{NND} is the ratio of the mean next neighbour distance for that field, d_{NN}, to the mean next neighbour distance for a random array of N_F particles in the field	0.64–1.24	0.08
Particle area, A_p (μm^2)	The area of a particle	0.01–0.21	0.002
Particle density,[c] ρ_p (μm^{-2})	The number of particles in a field divided by the area of the field	0.05–2.58	0.07
Particle diameter, d_p (μm)	The mean of 180 diameters of a particle measured from 0° through 179° in increments of 1°	0.20–0.62	0.01
Particle shape factor, F_S	The shape factor quantifies the "roundness" of a particle. It is defined as the area of the particle divided by the area of a circle of the same perimeter distance as the particle	0.35–0.45	0.02

[a] The minimum and maximum mean values from among all 19 samples (see text).
[b] The square root of the mean square error of all the replicate measurements.
[c] These field parameters are normalised to the MMT content of each nanocomposite sample, *M*, making them a "specific" fraction and density.

Fig. 6 presents several distributions of selected particle properties, clearly showing the differences in distributions among these properties. For example, the shape factor, F_S, has an approximately normal distribution and, therefore, may be adequately summarised by the arithmetic mean; in contrast, particle diameter, d_p, and particle area, A_p, show highly asymmetrical distributions. Consequently, it is worthwhile to briefly investigate the relative effectiveness of different statistics in summarising such highly non-normal distributions. Table 7 presents the data range and error, the data separation and the correlation with arithmetic mean of these different statistics of A_p across the 19 samples. Without discussing each statistic in detail, it is apparent that the higher-order moments of skewness and kurtosis, the maximum and lowest few percentiles, and the mode all fail to distinguish between any of the samples; this is due to small ratios of data range to error. Conversely, the maximum data separation occurs for the mean value. High levels of separation also occur for $P_{97.5}$, $P_{99.5}$ – due to the much larger ratio of data range to error compared with P_{100} – and the standard error. Interestingly, these latter statistics all show strong correlations with the mean; even the remaining statistics, which only show intermediate values of data separation, have at least moderate correlations with the mean. Given these generally strong correlations, and the ability of the mean to best distinguish among samples, we will use arithmetic means to summarise the distributions of particle parameters. The data ranges shown in Table 6 are mean values.

The analysis of data separation for the particle and field properties, as summarised in arithmetic means, is presented in Table 8. It is evident that, of the eight properties selected, only d_p, d_{NN}, A_p and ρ_p show even low-to-moderate levels of data separation. The fact that 36% of pair-wise differences for d_{NN} are significant at $\alpha = 0.05$ is suggestive of some potentially important variations in the spatial arrangements of microstructure in the nanocomposites. However, this is not necessarily true because d_{NN} depends not only on spatial arrangement of particles, but also on the particle density, ρ_p: the distance between particles decreases with increasing number of particles. This relationship has been noted by Fornes and co-workers [53,74] in the high-magnification structure of extruded nylon nanocomposites. Normalising d_{NN} to give r_{NND} accounts for the effect of ρ_p. Clearly, on the basis of r_{NND}, there are no statistically significant differences across the 19 samples in terms of particle arrangement. This also indicates that the differences in d_{NN} are merely reflections of the changes in ρ_p, rather than the effect of any significant difference in spatial arrangement of particles. Consequently, only d_p, A_p and ρ_p seem to be the promising summary parameters for the microstructure of the nanocomposite samples. We would expect a positive correlation between d_p and A_p, while conservation of mass indicates that these two parameters

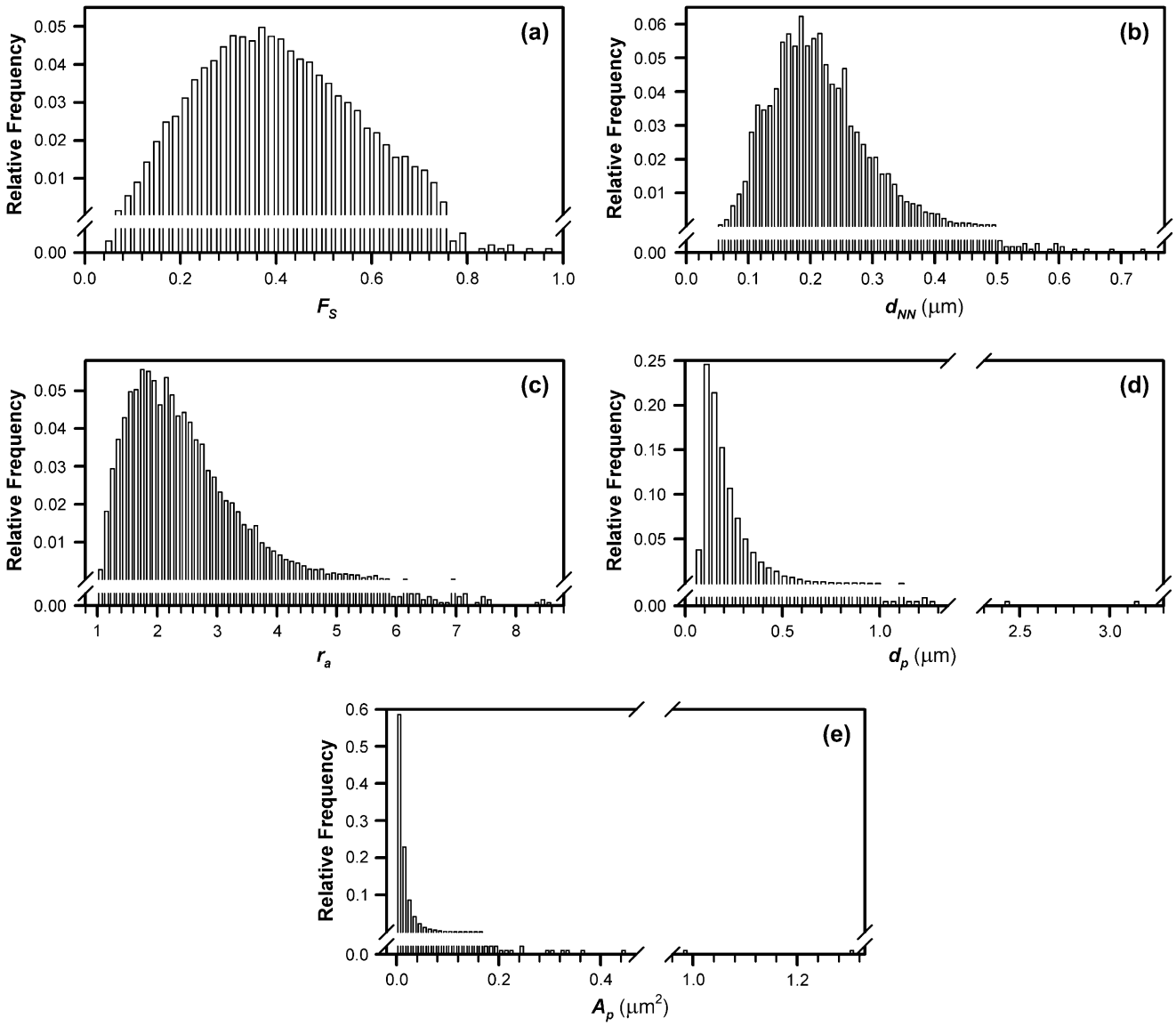

Fig. 6. Example distributions of particle properties for a single nanocomposite: (a) shape factor, F_S, (b) next neighbour distance, d_{NN}, (c) aspect ratio, r_a, (d) particle diameter, d_p, and (e) particle area, A_p.

should have some type of inverse relationship with ρ_p. Under the simplifying assumptions of monodisperse, spherical particles of constant physical density (which are, at best, tenuous for the MMT particles), stereological considerations of projected images [75,76] allow it to be shown that ρ_p should be proportional to A_p^{-1} and d_p^{-2}. The correlations between these parameters are given in Table 9. Two points are evident. Firstly, the inverted parameters, A_p^{-1} and d_p^{-2}, give better correlations with ρ_p than do A_p and d_p, in line with expectations from stereological principles. Secondly, A_p^{-1} and d_p^{-2} have moderate-to-good correlations with ρ_p, suggesting that it will be sufficient to use the field parameter ρ_p to quantify the microstructure of the nanocomposites. A visual correlation of sample structure with ρ_p is given in Fig. 7; it is obvious that there is an increase in the number of particles (or a decrease in mean particle size) with ρ_p. This provides further confirmation of the suitability of ρ_p to parameterise the microstructures.

3.3. Comparison of high- and low-magnification data

Prior to using these new parameters to investigate the effects of specific processing conditions on PMMA–clay nanocomposite structure, it is worthwhile to briefly examine the possible correlations between the nanostructural and microstructural parameters presented above. Table 10 clearly shows that the correlations between the nanostructural and microstructural parameters range from poor to moderate; the worst correlations occur for SE_n^{-1} (mean $r^2 = 0.10$). Overall, the highest r^2 value is 0.58 between ρ_t and ρ_p, while the value for D_E and ρ_p is only 0.43. (Even if we consider all of the possible summary parameters that have already been excluded the largest r^2 value only increases to 0.69 for ρ_t and r_{NND}.) Graphing the data illustrates that there are positive trends between the high- and low-magnification parameters, but these are not sufficiently strong to allow characterisation to

Table 7
The data ranges and errors of selected statistics of particle area, A_p, along with the analysis of their data separation and their correlation coefficients with arithmetic mean

Summary statistic for particle area[a]	Data range[b] (μm^2)	Error[c] (μm^2)	P-value[d]	Proportion of significant pair-wise differences[e] (%)	Correlation coefficient, r^2, with mean
Kurtosis	50–3000	1000	0.9643	0	0.028
Skewness	5–50	13	0.9297	0	0.018
P_0	0.0016–0.0032	0.0003	0.6321	0	0.0019
$P_{2.5}$	0.0025–0.0033	0.0005	0.3661	0	0.059
$P_{0.5}$	0.0021–0.0032	0.0003	0.3203	0	0.051
P_{100}	0.6–13.3	2.6	0.277	0	0.70
Mode	0.0003–0.0004	0.0003	0.2036	0	0.16
P_{10}	0.0030–0.0077	0.0002	0.0044	13	0.46
P_{25}	0.005–0.021	0.001	0.0006	16	0.55
Standard deviation	0.02–0.77	0.02	0.0003	26	0.97
Median	0.008–0.058	0.001	0.0002	26	0.70
P_{75}	0.016–0.145	0.003	<0.0001	27	0.92
P_{90}	0.029–0.438	0.006	<0.0001	35	0.99
Standard error	0.0001–0.0300	0.0002	<0.0001	37	0.88
$P_{99.5}$	0.10–3.53	0.05	<0.0001	37	0.99
$P_{97.5}$	0.06–1.96	0.02	<0.0001	43	0.94
Mean	0.014–0.210	0.002	<0.0001	46	1.00

The statistics are presented in order of increasing data separation, *i.e.*, by the fifth column.

[a] Kurtosis is a measure of the heaviness of the central peak – alternatively, the thinness of the tails – of the distribution. Skewness is a measure of the asymmetry, or sidedness, of the distribution. P_k, where k is a number between 0 and 100, represents the kth percentile. Thus, P_0 is the minimum value, P_{25} is the first quartile, P_{50} is the median, P_{75} is the third quartile, and P_{100} is the maximum value.

[b] The minimum and maximum values from among all 19 samples.

[c] The square root of the mean square error of all the replicate measurements.

[d] From one-way ANOVA; null hypothesis is the difference between all means = 0.

[e] Out of an absolute total of 105 possible pair-wise differences, as tested at $\alpha = 0.05$ with the Tukey–Kramer multiple comparisons' test.

be simplified down to a single parameter (see Fig. 8 for example). Consequently, both D_E and ρ_p, as the key characteristic parameters of the nanostructure and microstructure, will be used in the discussion. There are two reasons for the relatively poor correlations. Firstly, the development of structure at the nanoscale and microscale tends to occur by different mechanisms, especially across a range of organoclays, which include reactive and unreactive modifiers, and two different types of processing. Secondly, different types of quantitative information are gathered at low and high magnifications. Thus, there is no consistent correlation among the 19 data points, but only a general positive scatter.

Table 8
Analysis of data separation across the mean particle and field properties used to summarise the microstructures of the 19 samples

Parameter	P-value[a]	Proportion of significant pair-wise differences[b] (%)
F_S	0.2658	0
r_{NND}	0.0664	0
r_a	0.0338	3
ϕ_A	0.024	4
d_p	0.0005	25
d_{NN}	<0.0001	36
A_p	<0.0001	39
ρ_p	0.0002	66

Parameters are presented in order of increasing data separation, *i.e.*, by the third column.

Notes: where, as defined in Table 6, ϕ_A is the area fraction, r_a is the aspect ratio, d_{NN} is the next neighbour distance, r_{NND} is the next neighbour distance ratio, A_p is the particle area, ρ_p is the particle density, d_p is the particle diameter, and F_S is the particle shape factor.

[a] From one-way ANOVA; null hypothesis is the difference between all means = 0.

[b] Out of an absolute total of 105 possible pair-wise differences, as tested at $\alpha = 0.05$ with the Tukey–Kramer multiple comparisons' test.

4. Discussion

Having obtained quantitative structural parameters from image analysis, we can use these parameters to investigate processing–structure effects in the PMMA nanocomposites. Before doing so, however, it is worthwhile to compare the outcomes of structural analysis from TEM with those from XRD, the most commonly used measure of structure in polymer–clay nanocomposites.

4.1. Comparison of structure as determined by XRD and TEM

XRD or WAXD provides an indication of the nanostructure within tactoids or agglomerates in polymer nanocomposites.

Table 9
Correlations between ρ_p and the other particle properties with proportions of significant pair-wise differences equal to or exceeding 25% in Table 8

Other parameter	Correlation coefficient, r^2
d_p	0.37
d_p^{-2}	0.62
A_p	0.34
A_p^{-1}	0.80

d_{NN} is excluded for the reasons outlined in the text.

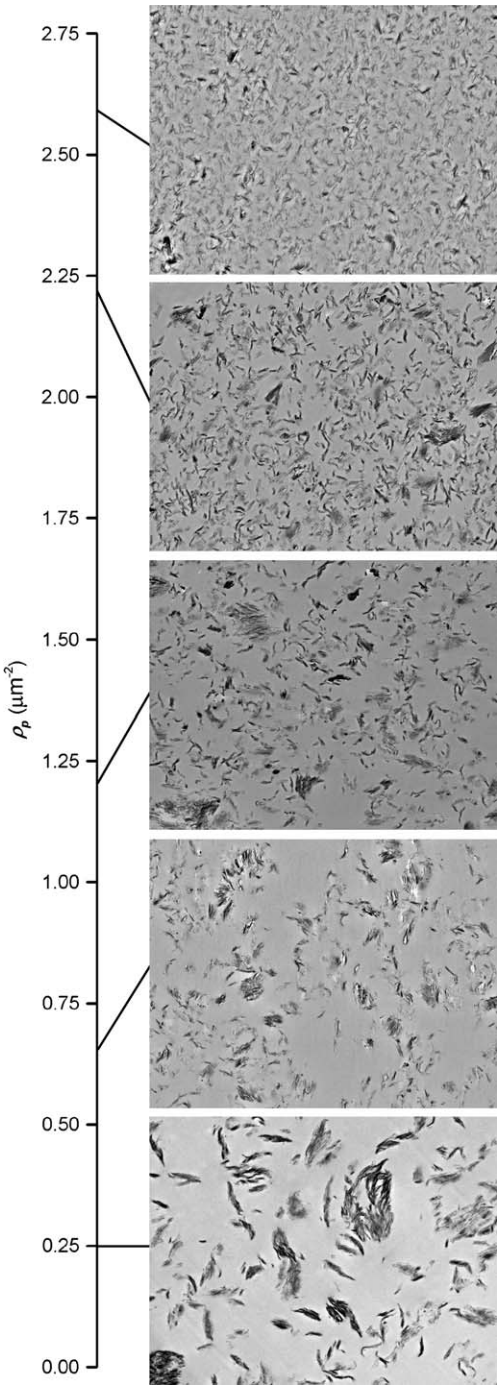

Fig. 7. Visual correlation of sample microstructure with particle density, ρ_p. The horizontal length of each field is 12.88 μm.

The position of the basal peak quantifies mean interlayer spacing, d_{001}, within particles; the area of the peak gives some estimate of the relative amount of layers existing in intercalated particles. The layer separations of the nanocomposites, d^{T}_{001}, were measured directly from the localised, high-magnification TEM images to allow direct comparison with the basal spacing, d^{X}_{001}, determined from the global measurements of WAXD. These two data sets are plotted in Fig. 9 and show good correlation with $r^2 = 0.94$. Therefore, as expected, the d^{X}_{001} values are representative of the mean basal spacing on the nanometre scale and, importantly, can be measured more rapidly and with far less effort than d^{T}_{001}.

Table 10
Correlations (r^2) of the parameters listed in Table 5 with A_p^{-1}, d_p^{-2} and ρ_p

	A_p^{-1}	d_p^{-2}	ρ_p
$\overline{n}^{-1}$	0.44	0.34	0.47
SE_n^{-1}	0.16	0.11	0.12
ρ_t	0.39	0.33	0.58
ρ_s	0.40	0.32	0.53
F_E	0.40	0.33	0.55
D_E	0.43	0.32	0.43
F_A^{-1}	0.50	0.34	0.46

Despite the utility of XRD, there remain three major limitations with the use of d^{X}_{001} as a parameter to characterise nanocomposite structure. Firstly, there is an upper limit to the distances that can be measured by WAXD. As is shown by the shaded region in Fig. 9, WAXD with Cu Kα radiation cannot detect platelet registry above approximately 6 nm because any basal peaks become undetectable in the rapidly increasing background intensity. Consequently, the two samples in this work that showed no basal peaks are considered

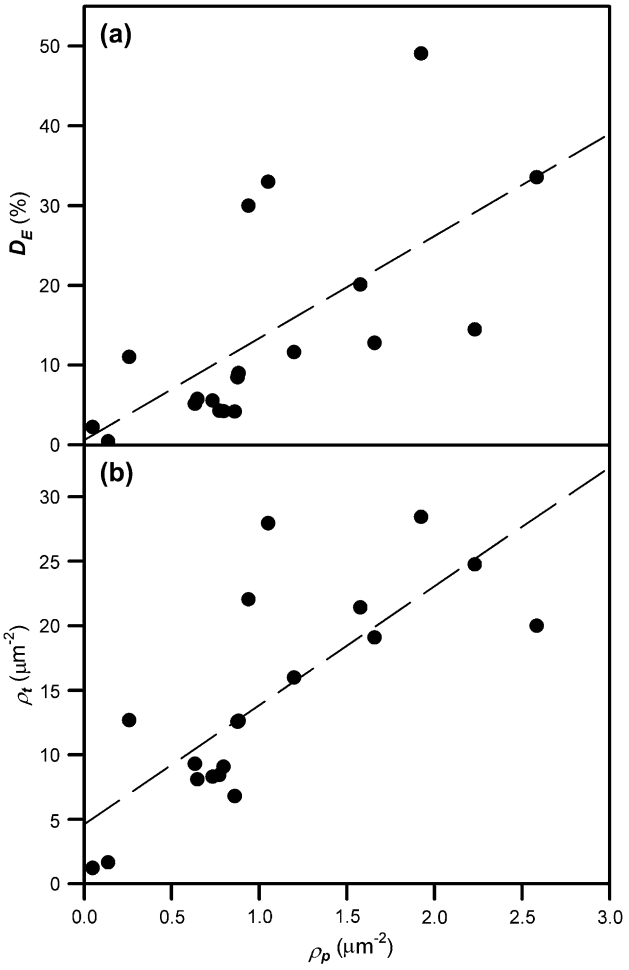

Fig. 8. Correlations between nanoscale and microscale parameters: (a) D_E and ρ_p and (b) ρ_t and ρ_p.

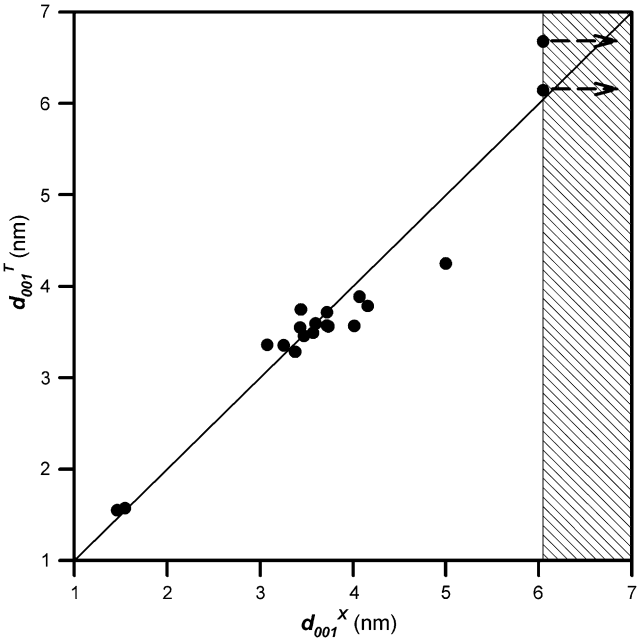

Fig. 9. Correlation of basal spacing distances determined from TEM image analysis, d_{001}^{T}, and XRD measurements, d_{001}^{X}. The shaded region represents layer separations that cannot be determined by XRD measurement; the arrows indicate that the adjacent points are nominal, lower-bound d_{001}^{X} values.

"exfoliated" by the WAXD definition. However, the corresponding d_{001}^{T} data in Fig. 9 along with the image analysis data show that those two samples, despite a moderate degree of exfoliation, have approximately 67% and 70% of layers in tactoids and agglomerate with mean layer separations of 6.14 and 6.68 nm, respectively. This is far from the fully "exfoliated" structure that might be assumed on the basis of the XRD data.

Secondly, WAXD cannot provide any measure of the number and separation of single layers, which represent the truly exfoliated structure at the nanometre scale. By way of illustration from this work, the best correlation of d_{001}^{X} with any exfoliation parameter is $r^2 = 0.33$ for F_E, while r^2 is reduced to 0.19 for D_E. On this basis, the use of basal spacing as a measure of exfoliation can be misleading. Some specific examples will further highlight the problems with interpreting d_{001}^{X} in terms of degree of exfoliation. As mentioned above, the two samples showing no basal peaks have D_E values of only approximately 30%; conversely, the sample showing the largest amount of exfoliation, $D_E = 49\%$, still has a significant diffraction peak at $d_{001}^{X} = 3.44$ nm. Clearly, d_{001}^{X} does not provide an accurate insight into all aspects of the nanostructure of polymer–clay nanocomposites. (It is possible in some situations to correlate the increase in background intensity of diffractograms with increasing degrees of exfoliation in nanocomposites [71]. However, this approach is only valid and accurate under extremely restrictive conditions.)

Thirdly, WAXD cannot determine whether any basal peaks observed arise from well-separated, small tactoids or from poorly dispersed tactoids clustered into large agglomerates; in other words, it is insensitive to nanocomposite microstructure. This is illustrated by the poor correlation of d_{001}^{X} with ρ_p at $r^2 = 0.073$. Even with comprehensive, *ab initio* modelling of the diffraction process [22], it is questionable whether an accurate estimate of the mean number of platelets per tactoid, $\overline{n}_X$, can be obtained from experimental XRD data given (i) the low volume fractions of MMT typically incorporated into nanocomposites and (ii) that peak shape is affected by both the range of intercalation distances and the range of platelet numbers per tactoid. Should an acceptably accurate estimate of $\overline{n}_X$ be obtained, this still can provide no insight into how those tactoids are arranged in the nanocomposite structure, whether as distinct, well-separated tactoids or large agglomerates of the smaller tactoids. Thus, XRD cannot quantify the microstructure of nanocomposites. These conclusions are consistent with the assessment that WAXD is not a stand-alone characterisation method and should be used in conjunction with TEM [22,28].

4.2. Effect of processing on nanocomposite structure

Three key parameters will be used to assess the effect of processing conditions on the structure of the PMMA nanocomposites. Two of these are the image analysis parameters D_E and ρ_p, which characterise the nanostructure and the microstructure of the nanocomposites, respectively. The third parameter will be Δd_{001}, the difference between the basal spacing of the nanocomposite and the original organoclay. (Where multiple basal peaks occurred in the organoclay, the effective mean d_{001} value listed in Table 2, *i.e.*, third column from right, was used to determine Δd_{001}.) In light of the discussion in Section 4.1, this parameter is used not only with the recognition of its limitations in quantifying nanocomposite structure, but it is also used with the awareness of the prevalence of WAXD in characterising polymer–clay nanocomposites. Like D_E, Δd_{001} also quantifies the nanostructure of the nanocomposites, but only in terms of the extent of intercalation of MMT layers that maintain registry at distances of less than approximately 6 nm. Together, these three parameters have been chosen to characterise different aspects of nanocomposite morphology at the nanoscale and microscale levels. We will use them, through a series of specific sample comparisons, to assess the effect of processing on the structure in PMMA nanocomposites. To simplify the statistical analysis of the discussion, the commonly used but somewhat arbitrary standard P-value of 0.05 will be taken as the boundary for "statistically significant" differences. Where possible (*i.e.*, for pair-wise comparisons), we also will consider the P-values from the application of the Kolmogorov–Smirnov test to the distributions of platelet number per particle as confirmation (or otherwise) of the trends in D_E.

4.2.1. Effect of the presence of organic modifier

The use of an organic modifier for the clay surfaces increases the compatibility between the otherwise hydrophilic clay and the more hydrophobic monomer and polymer. Unsurprisingly, therefore, the use of an organoclay (H99) compared with the unmodified clay (MMT) leads to improved structure on the basis of all three parameters as shown in Fig. 10. The

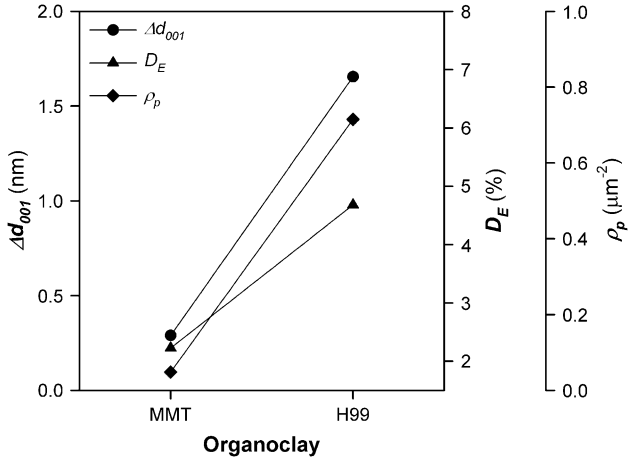

Fig. 10. Effect of presence of an organic modifier on nanocomposite structure; MMT has no organic modifier (Na^+ ions), H99 contains HTA^+ ions (sample names refer to the organoclays listed in Table 2).

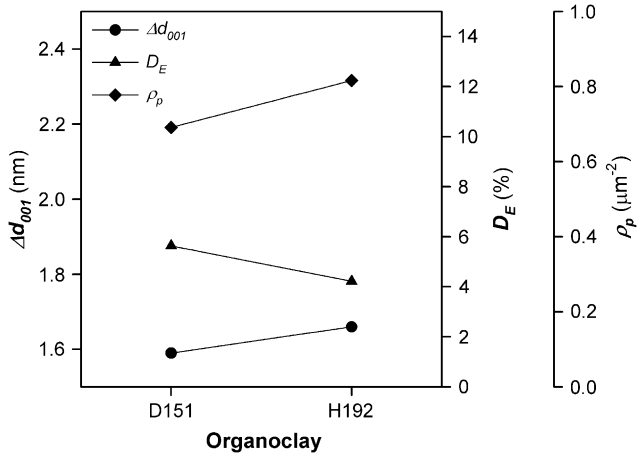

Fig. 11. Effect of tail length of conventional, alkyl ammonium surfactants on nanocomposite structure; D151 contains DTAB with a tail length of 12 carbons, H192 contains HTAB with a tail length of 16 carbons.

corresponding *P*-values from a one-way ANOVA are less than 0.001 for Δd_{001}, 0.003 for ρ_p and 0.01 for D_E, indicating the significance of these trends. Obviously, the presence of hexadecyltrimethylammonium (HTA^+) ions increases monomer intercalation and polymer compatibility, thereby causing a large increase in Δd_{001}. Likewise, these modifiers enhance the dispersion and gelation of the organoclay; for example, the gel volumes in MMA of these two organoclays were 22% for MMT and 66% for H99. This improved dispersion naturally reduces the mean particle size and increases ρ_p. None of this is surprising. The truly noteworthy point is that, in contrast to the large changes observed in Δd_{001} and ρ_p, which approach or exceed an order of magnitude, the difference in D_E is less than double. In fact, the application of Kolmogorov–Smirnov test to the distributions of platelet number per particle gives a *P*-value of 0.29, indicating no statistically significant difference between the nanostructure of the MMT sample and H99 sample as quantified in the entire distribution, rather than D_E. There are two reasons for this relatively small effect. Firstly, the absence of modifier does not prevent limited exfoliation of MMT layers (approximately 2.5%) – this agrees with the ready intercalation of MMA vapour into Na-MMT observed by Blumstein and co-workers [77–79]. Secondly, and probably more importantly, though the conversion of the MMT to alkyl ammonium organoclay increases intercalation significantly, it has a relatively small effect on exfoliation. This conclusion is consistent with work showing that higher levels of exfoliation require either reactivity – *i.e.*, intragallery polymerisation – in bulk-polymerised systems [2,16,19,80] or else tailoring of the (co-)polymer chemistry (polarity and affinity) to novel organoclays [81]. In other words, it is necessary to do more than simple alkyl ammonium modification of MMT to obtain significant improvements in exfoliation.

4.2.2. Length of alkyl tail of modifier

Fig. 11 shows slight trends for the three parameters with an increase in alkyl tail length from 12C (D151) to 16C (H192); however, there are essentially no statistically significant effects. At 0.049, the *P*-value of D_E shows borderline significance, but the Kolmogorov–Smirnov test suggests otherwise with a *P*-value of 0.76 for the comparisons of the entire distributions. Both Δd_{001} and ρ_p have *P*-values larger than 0.25. The absence of strong effects of alkyl tail length is reasonable as all modifiers examined in this work had tails longer than the 10–12 carbons necessary to impart true organophilic character to the organoclay [68,82]. At and above this limit, the length of the tails affects the basal spacing of organoclay, but does not particularly modify the degree of compatibility. This finding is consistent with work by Fornes et al. [51] showing that the length of alkyl tails had no significant effect on morphology or mechanical properties of extruded nylon-6–Cloisite nanocomposites at lengths of 12, 18 and 22 carbons. Similarly, for tail lengths of 12 or more carbons, Reichert et al. [83] found that the mechanical properties and nanostructure of melt-compounded poly(propylene) was relatively insensitive to tail length.

4.2.3. Effect of parent clay type

Several studies have demonstrated that differences in the properties of the layered silicates – in particular, the cation exchange capacity (charge density) and morphology (platelet size) – can influence final nanocomposite structure [2,71,80,84]. In this work, the two parent clays have similar layer charge densities, but different distributions of platelet lengths (see Fig. 3); these differences in platelet dimensions might be expected to influence the nanocomposite structure. To assess this effect, Fig. 12 compares the trends for samples made from stoichiometric organoclays derived from bentonite (H99) and Cloisite (C30B), which have similar, but not identical, modifiers. Naturally, the difference in moieties on the quaternary groups on the modifiers – the polar bis-2-hydroxyethyl groups of C30B and the methyl groups of H99 – might account for at least some of the trends observed in Fig. 12 and, therefore, confound the effect of platelet size. Certainly, the literature shows that hydroxyethyl groups have some effect on nanocomposite structure and/or properties in melt-compounded

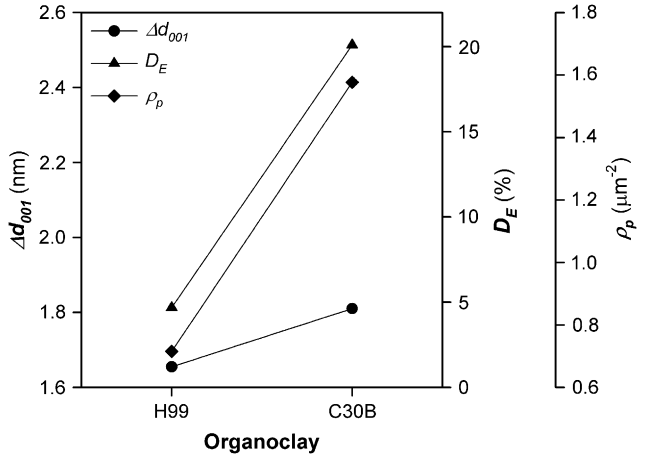

Fig. 12. Effect of parent clay type on nanocomposite structure; H99 is derived from the bentonite clay, C30B is made from Cloisite Na.

systems, whether the effect is beneficial or detrimental depends strongly on the nature of the polymer involved. For example, the presence or absence of hydroxyethyl groups had little effect on structure as visualised by TEM in nylon-6 [51] or polycarbonate [43], though mechanical properties changed. In contrast, hydroxyethyl groups appreciably increased exfoliation and improved properties in poly(ethylene-*co*-methacrylic acid) ionomers [52]. Of these three systems, the nylon-6 and polycarbonate likely provide a better guide to the expected effect of hydroxyethyl groups on the structure in PMMA nanocomposites than the relatively nonpolar polyethylene ionomer. Consideration of solubility parameters for nylon-6, polycarbonate, PMMA and polyethylene supports this argument [85]. Therefore, it seems reasonable to conclude that any trends observed in Fig. 12 are probably due more to the differences in the platelet sizes of the organoclays than to the presence or absence of hydroxyethyl groups on the modifiers.

It is evident from Fig. 12 that both samples show large shifts in d_{001}, but by approximately the same amount ($\sim$1.7 nm) such that there is no statistically significant difference in Δd_{001} (P-value larger than 0.25). This is to be expected if there is no real difference in compatibility derived from the two modifiers, because ultimately the chemical compatibility between the organoclay and polymer controls the extent of layer separation [3]. Thus, the Δd_{001} data also support the conclusion that the hydroxyethyl groups likely have limited effect on the structure in the system. In contrast to Δd_{001}, D_E and ρ_p show large increases from H99 to C30B with P-values less than 0.001 in each case. The Kolmogorov–Smirnov test on the high-magnification distributions also produced a P-value less than 0.001, supporting the significance of the trend in D_E. The major difference between these two organoclays is the difference in platelet size of the clays. Specifically, the H99 has a maximum platelet length of 574 nm and a mean of 85 nm; the C30B has a maximum platelet length of only 234 nm and mean of just 58 nm. It seems possible that the structural differences between H99 and C30B are predominantly due to the large variation in platelet size of the parent clays. For instance, Kumar et al. [86] have stated that platelet size affects the dispersion of organoclay in a polymer matrix during extrusion. It is also known that smaller platelet sizes lead to greater gelation in MMT suspensions [87,88]. This is consistent with the gel volume data measured here in MMA, which were 66% for H99 and 91% for C30B. Thus, the significantly smaller platelets in C30B allow greater microscale dispersion (*i.e.*, smaller tactoids) and greater nanocale dispersion (*i.e.*, more exfoliation) as evinced by the gel volume data. Evidently, at least some of this relative difference in structure is retained during polymerisation, giving larger D_E and ρ_p values for the C30B sample compared with the H99 sample. Of course, the other complicating factor is the residual nanoscale cristobalite associated with the bentonite samples, which cannot contribute to the gel structure and, therefore, likely reduces the overall gel volumes.

The importance of the difference in platelet sizes of the two parent clays is also shown by plotting the gel volumes of the bentonite and Cloisite organoclays in MMA as a function of ΔHLB, which provides a theoretical indicator of compatibility between the organoclay and MMA (Table 2). The hydrophile–lipophile balance (HLB) concept and its application to assess compatibility in organoclay–monomer systems have been detailed elsewhere [63], but essentially it involves matching the HLB of the surface modifiers, HLB_D, to the optimal HLB of the monomer–clay system, HLB_O. The closer the match between HLB_D and HLB_O, the more compatible, and therefore exfoliated, the organoclay should be in the MMA. In this case, ΔHLB quantifies the absolute difference between HLB_D and HLB_O. Fig. 13 presents the gel volumes in MMA as a function of ΔHLB for the unreactive organoclays and clearly shows that the data for the bentonite organoclays and the Cloisite organoclays fall onto entirely different lines. Moreover, the

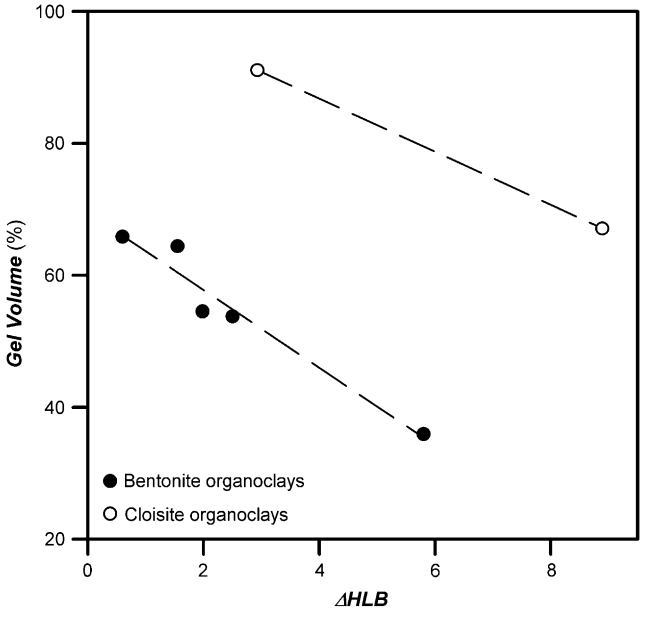

Fig. 13. Plot of gel volumes in MMA as a function of ΔHLB for the unreactive organoclays; two distinct lines of data are evident on the basis of the two parent clays.

line for the Cloisite organoclays lies significantly above that for the bentonite organoclays, as expected from the difference in platelet dimensions of the two parent clays. These data confirm the importance of platelet dimensions in controlling the initial ''nanocomposite'' structure prior to polymerisation. They also exclude the presence of the hydroxyethyl groups as the main reason for the structural difference between the H99 and C30B samples, as was discussed above.

4.2.4. Effect of reactivity of modifier

The incorporation of a reactive modifier within the MMT galleries, whether as an initiator or simply as a polymerisable surfactant, is known to increase platelet separation during polymerisation [1–3,16,17,89]. Therefore, we might expect all the structural parameters to improve in the sample containing the reactive surfactant (*i.e.*, MH151); this is seen to be the case in Fig. 14. As discussed by Zeng and Lee [3], use of polymerisable modifiers increases intragallery polymerisation, which tends to drive the platelets farther apart and increase exfoliation. Hence, Δd_{001}, which measures layer separation, and D_E, which measures exfoliation, both increase significantly in Fig. 14 (both parameters give *P*-values less than 0.001 as does the Kolmogorov–Smirnov test on the high-magnification distributions). Although ρ_p increases, the increase is not statistically significant (*P*-value is greater than 0.25); this shows a negligible difference between these two samples, despite the large differences in nanoscale structure. Although this might seem counterintuitive, this lack of difference arises because the reactivity is very much a nanoscale phenomenon and doesn't translate to differences in microstructure for the following reasons. Firstly, although the reactive surfactants increase separation of layers (by at least 2–3 times) compared with non-reactive surfactants, these expanded tactoids tend to retain the registry of the layers. This result is consistent with the images presented for epoxy nanocomposites in which the organic modifiers participated in the curing reaction; the resulting structure comprised aligned layers separated by

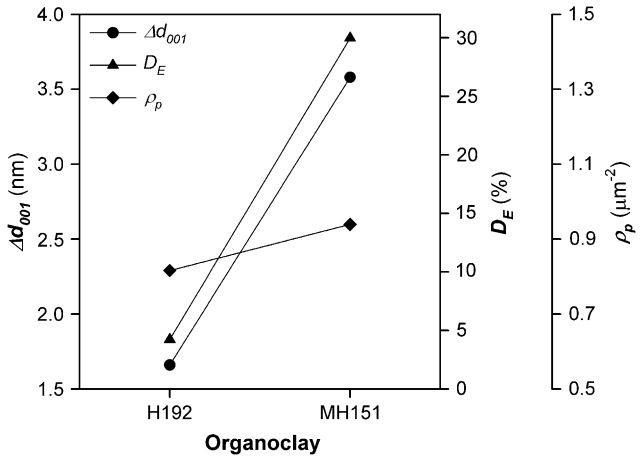

Fig. 14. Effect of reactivity of modifier on nanocomposite structure; H192 contains a conventional surfactant (HTAB), MH151 contains a reactive surfactant (MEHDAB).

10–15 nm [89] or 10–20 nm [16]. The consequence of this retained registry is that the apparent tactoid structure is still evident at lower magnifications, even in reactive systems. For example, the edge size of a pixel is 13 nm at 7100× magnification; given that at least several pixels are required to distinguish structure, the minimum distance for observable structure is approximately 50 nm. Clearly, the changes in layer separation caused by the reactive surfactant are essentially undetectable at low magnification. Secondly, the reactive surfactant also significantly increases the number of single layers (*i.e.*, D_E), but most of the individual platelets are not visible at the micrometre scale; again, therefore, the samples appear similar at low magnification.

Notice that these two effects are competitive in terms of their overall influence on the microstructure. Specifically, the increase in basal spacing within ''tactoids'' in the MH151 system leads to an increase in the apparent area fraction of particles at low magnifications; *i.e.*, more intercalated polymer is perceived as ''particle.'' Conversely, the corresponding increase in exfoliation decreases the amount of MMT detectable at low magnifications, which decreases the area fraction of clay. Evidently, the former effect predominates because the mean specific area fractions of the MH151 and H192 samples, respectively, were 3.20% and 2.85%. In other words, microstructure seems to be controlled more by efficiency of dispersion than by the reactivity of systems, although this is a highly influential factor at the nanometre scale. If this is the case, the gelation behaviour of the two organoclay systems in MMA should be similar, in accord with the small variations in ρ_p. The gel volume for MH151 in MMA was 53%; on the basis of the data for H99 and H192, the interpolated gel volume for ''H151'' is 49%, which is very similar to that measured for MH151.

4.2.5. The effect of excess modifier

Excess modifier readily becomes trapped in organoclays as organic salt during the cation exchange of long-chain organic cations [49,50,82,90–103], when the alkyl tail is longer than approximately nine carbons [94]. This phenomenon is attributed to hydrophobic bonding, the mutual attraction among the alkyl chains that arises from the tendency of water molecules to minimise contact with these hydrophobic moieties [49,97,104,105]. It is possible to avoid entraining excess organic salt by using only the exact amount of organic cations necessary for stoichiometric exchange during the cation exchange process [82,97,101,106]. Alternatively, the excess organic salt can be removed by washing the organoclays in polar organic solvents such as alcohols [49,96] or trichloromethane [90].

It is known that excess organic salt significantly alters the properties of the organoclays; excess salt is often added to commercial organoclays to modify their solvation and gelation behaviour and rheological properties [100,103]. However, the exact effect of excess organic salt remains unclear, because excess modifier can influence the behaviour of organoclays dispersed into organic solvents or monomers in opposite ways. Mandalia and Bergaya [107] found that the gel volumes of organoclays in nitrobenzene increased approximately linearly

with the amount of excess modifier. Consistent with this, He et al. [108] observed slightly larger swelling volumes for a montmorillonitic organoclay before Soxhlet extraction than afterwards, once the excess salt was removed. Likewise, Sobisch and Lerche [109] noted that excess modifier is used as an "activator" to enhance organoclay dispersion; they found that the organoclay containing excess surfactant produced larger gel volumes in cyclohexane. In contrast, Moraru [110] showed that the yield strength of organoclay gels in toluene decreased as the amount of excess organic salt increased. Also, Ho et al. [103,111] qualitatively noted that removal of excess salt from organoclays increased their propensity to gel in organic solvents. Trends in solvent absorption are also variable. For example, Slade and Gates [66] found that excess organic salt in organoclay increased absorption of aromatic solvents, while Bonczek et al. [104] noted a reduction in solvent uptake at 50–100% excess modifier. Some of these apparently conflicting results are caused by the different measures of organoclay–solvent interaction used in the literature; for instance, gel volume and gel strength need not be correlated parameters. Other reasons for these discrepancies relate to differences in clay, modifiers and solvents used in the various studies as well as differences in the amount, and possibly location, of excess modifier in the organoclays. Moreover, the dispersion and gelation of organoclay in organic solvents are complex processes, governed by the balance of cohesive and solvation energies in the organoclay as well as the electrostatic forces, which are particularly influenced by excess organic salt, and the entropic effects in the system [110].

Similar uncertainty is associated with the role of excess modifier in the development of final nanocomposite structure. Some workers have suggested that the more open organoclay structure derived from excess modifier should enhance exfoliation during nanocomposite synthesis [112,113]. Certainly, Shah et al. [52] observed that the extrusion of an organoclay with approximately 45% excess organic salt improved the mechanical properties of a poly(ethylene-*co*-methacrylic acid) ionomer beyond that observed with the stoichiometric organoclay. Mandalia et al. [107] concluded that the best properties of polyethylene and poly(ethylene vinyl acetate) nanocomposites occurred when the incorporated organoclay contained 20–50% excess surfactant. Morgan and Harris [113] observed that excess modifier was necessary for intercalation of polypropylene into the organoclay tactoids during extrusion. Conversely, they found that the excess salt seemed to decrease the overall quality of the tactoid dispersion as assessed from TEM micrographs [113]. Similarly, Fornes et al. [51] concluded that approximately 30% excess organic salt in an organoclay reduced the ease of platelet dispersion in extruded nylon-6 nanocomposites. In another study of extruded nylon-6 nanocomposites, Garcia-Lopez et al. [112] also concluded that exfoliation seemed to increase when the amount of excess surfactant in the organoclay was reduced. Likewise, Panek et al. [114] tentatively concluded that excess organic salt in organoclays lessened the tendency for poly(styrene) to penetrate the galleries of the organoclay during melt intercalation. Again, at least some of these apparently conflicting findings are because of the different systems used in these studies, which lead to different interactions among the polymer chains, the surface modifiers and any exposed silicate surface [52]. In any case, these previous findings are solely from melt-processed systems, making them of questionable relevance to this work where the effect of excess salt is examined in bulk-polymerised PMMA. Of more direct bearing to this work is a study by Lee and Kim [50] of HTA-MMT organoclays containing no excess and a significant excess of organic salt. From a TEM examination of sections of resin-embedded organoclay (*i.e.*, resin nanocomposites), it was suggested that organoclays containing excess organic salt might show enhanced exfoliation, especially on platelets with lower charge densities. We note, however, that the TEM specimen preparation technique used by Lee and Kim [50] – equilibration in and replacement of 2:1 ethanol–resin (twice) and resin only (four to six times) before curing – would have leached at least some of the excess salt from the samples (see the foregoing discussion of organoclay washing and the results of reference [66]). Consequently, the samples examined by TEM cannot be considered as representative of 150% excess salt. Nonetheless that study by Lee and Kim [50] suggests that excess salt might enhance structure in the bulk-polymerized nanocomposites.

The main effect of excess organic salt in bulk-polymerised PMMA nanocomposites is shown in Fig. 15. It is evident that D_E and ρ_p increase slightly from no excess to medium excess followed by a large increase to high excess; both parameters show a high statistical significance overall with *P*-values of less than 0.001. Clearly, an excess of organic salt, particularly a large excess (*i.e.*, greater than 100% of organic salt), increases the degree of microscale dispersion and nanoscale exfoliation. Although, as outlined above, the observed influence of excess modifier varies, we would expect that the dispersion of the organoclays into MMA would be enhanced by the excess salt for the following reasons. Firstly, it is known that increasing the initial basal spacing in the organoclay reduces the attractive forces among the platelets, which tend to enhance delamination [50,53,109]. Secondly, the excess modifier also

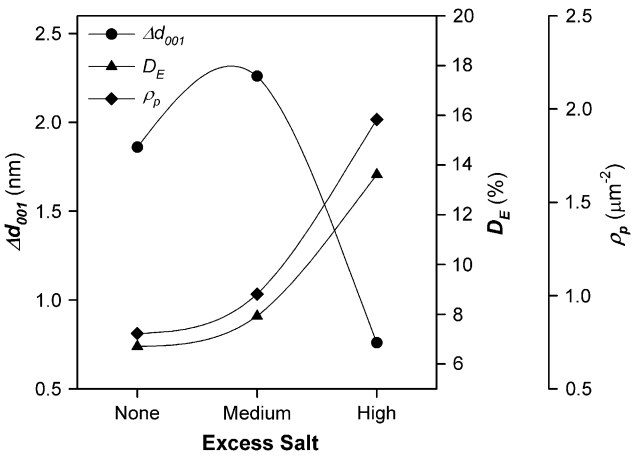

Fig. 15. The main effect of excess organic salt (modifier), varying from stoichiometric exchange to medium excess (mean salt content of 65%) to high excess (mean salt content of 149%).

is occluded in the pores within the agglomerates and on the surfaces of the tactoids [112,115]; this tends to open up the organoclay structure and increases the ease of dispersion of the tactoids and reduces the mean size of the tactoids [109]. Thirdly, excess salt increases electrostatic repulsion among the organoclay particles, thereby increasing suspension stability [110], consistent with the commercial use of excess modifier in organoclays to encourage dispersion in solvents [103]. Importantly, this last effect might also reduce the extent of particle re-agglomeration during polymerisation of the MMA, which would tend to further increase D_E and ρ_p in the final nanocomposites. Despite the issues associated with the specimen preparation technique used by Lee and Kim [50] outlined above, the trend in Fig. 15 is also consistent with their findings of increased exfoliation of organoclays containing excess salt.

The trend for Δd_{001} differs from that observed for D_E and ρ_p; Δd_{001} increases from no excess to medium excess, but drops thereafter (P-value less than 0.001). The initial increase is consistent with excess salt increasing the ease of further layer expansion, congruent with the increase in D_E and ρ_p discussed above. The subsequent drop in Δd_{001} at high excess probably occurs for two reasons. Firstly, the denser and more ordered packing of the modifier chains at high excesses possibly reduces the driving force for monomer and polymer intercalations. For example, Mandalia and Bergaya [107] found that the intercalation of molten polyethylene, as measured by the final basal spacing, was slightly less when the organoclay contained 100% excess salt than for the organoclay with 50% excess salt. They attributed this to more favourable entropic interactions of the polymer chains with the more mobile and disordered modifiers in the organoclay that contained less excess organic salt. In the current work, the mean relative basal spacings, normalised to those of the stoichiometric organoclays, were 14% larger for medium excess and only 2% larger for the high excess. Clearly, these entropic factors, the gallery accessibility, and the leaching of free surfactant into the MMA all alter the final compatibility in the PMMA, thereby limiting the final basal spacing at the highest amounts of excess modifier. However, the second and probably the main reason for the large drop in Δd_{001} at high excess is that the organoclays with the high excess of salt already start with strongly expanded layers due to adsorption of excess salt into the hydrophobic galleries (mean $d_{001} \sim 3.1$ nm). In consequence, the increase in d_{001} in the nanocomposite (*i.e.*, Δd_{001}) is much smaller than for the less-expanded organoclays. This effect has been observed by Fornes et al. [51] during the extrusion of nylon-6 nanocomposites and by Lee et al. [116] during melt intercalation of poly(styrene-acrylonitrile). In both cases, the final d_{001} values were very similar for the nanocomposites containing stoichiometric and over-exchanged organoclays. However, because the initial d_{001} values for the over-exchanged organoclays were much larger than those for the stoichiometric organoclays, smaller Δd_{001} values resulted in the systems containing excess salt. Fornes et al. [51] also noted that there was a high likelihood of migration of free modifier molecules from the interlayers during the extrusion process, such that the organoclay tactoids and platelets became more similar to those of the stoichiometric organoclay; of course, this would lead to a significant underestimation of Δd_{001}. The same holds true in this work where some leaching of modifiers into the MMA would have occurred during sonication so that the apparent drop in Δd_{001} from medium excess to high excess probably is exaggerated.

Overall, these main effect data indicate that the key structural features of PMMA nanocomposites are improved by a significant excess of organic salt in the organoclay, which likely enhances the separation of tactoids and layers and better stabilises the suspended particles. Despite these potential structural benefits, however, the practical benefits of such an approach are limited. For example, the addition of a very large excess of surface modifier will add to the overall cost of the organoclay per unit mass. Additionally, it is probable that some of the excess modifier will leach or migrate from the organoclay into either the monomer (bulk polymerisation) or molten polymer (extrusion); this free surfactant is likely to have adverse plasticising effects on the mechanical properties of the final nanocomposites [51,113,116].

4.2.6. Effect of processing and organoclay type

It is known that significant differences in processing or synthesis methods or large variations in organoclay type (*i.e.*, surface modifier) can lead to major changes in nanocomposite structure. In this work, the samples made by bulk polymerisation and extrusion that contain C30B and C93A organoclays form a 2^2 factorial design in the factors (1) processing and (2) organoclay type. Therefore, analysis of these data allows exploration of the main effects of processing and organoclay type and of the interaction between these two factors; these data are presented in Fig. 16. Considering, the effect of processing method first, it is clear that structure develops entirely differently by these two methods. Prior to bulk polymerisation, the organoclays are dispersed into the MMA by extended sonication, thereby forming highly dispersed gel structures (with the extent of gelation controlled by chemical compatibility). As a consequence of this initial gel structure, the bulk polymerisation process for conventional organoclays is one in which the structure actually deteriorates during polymerisation, as decreasing compatibility [117,118] and the forces of extragallery polymerisation [2,80] tend to drive the tactoids and platelets together to give the final nanocomposite morphology. In contrast, the extrusion process starts with large organoclay agglomerates and improves the structure by intercalating the polymer, breaking the agglomerates into tactoids and subsequently peeling away individual, or small groups of, layers by means of viscous shear forces [4].

The main effect of these different processing methods on final structure is presented in Fig. 16 (left). Evidently, D_E and ρ_p are much larger in the extruded samples than in the bulk-polymerised samples; both have P-values of less than 0.001. This result is not surprising given that extrusion is a kinetic process that uses shear forces in the viscous polymer melt to increase delamination of the layers [4,5]. Moreover,

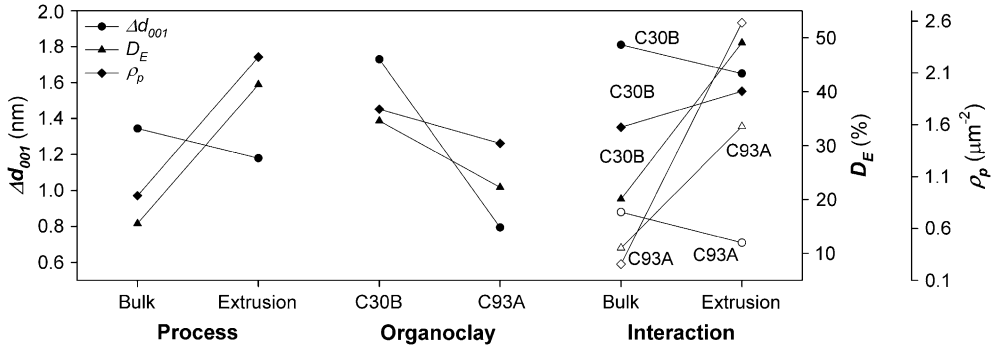

Fig. 16. Main effects of synthetic process (bulk polymerisation versus extrusion) and organoclay type (C30B versus C93A) and their interactions.

Dennis et al. [4] found that these shear forces are the dominant reason for the breakdown of the initial organoclay agglomerates into smaller tactoids (or intercalates); therefore, shear also accounts for the significantly higher ρ_p values in the extruded samples. Vermogen et al. [37] have seen similar effects.

On the other hand, Δd_{001} shows a small, probably insignificant trend in the opposite direction (P-value = 0.109); *i.e.*, there are slightly greater layer separations in the bulk-polymerised samples than in the extruded samples. Though not significant, this trend can be understood in terms of the very different nature of structural development by these two processing routes, as explained above. In essence, bulk polymerisation represents at least some structural collapse from the more dispersed gel of the organoclay in the monomer. Conversely, extrusion involves intercalation of the molten polymer between the platelets, as well as the breakdown of agglomerate and tactoid structures. Therefore, as synthesis proceeds, Δd_{001} decreases in the samples made by bulk polymerisation [67,80], whereas Δd_{001} increases in the samples made by extrusion. The respective structural development ceases when the glass transition temperature (T_g) of the growing PMMA chains attains the reaction temperature during bulk polymerisation, and when the molten nanocomposite exits the extruder. Thus, it is entirely possible for the final layer separation to be slightly greater in the bulk-polymerised samples than in the extruded ones, depending on the relative degree of layer collapse and expansion, respectively, at which structural evolution stops.

The main effect of organoclay type in Fig. 16 (middle) shows that all parameters have highly significant trends with a decrease in nanoscale and microscale exfoliation from C30B to C93A (P-values: $\Delta d_{001} < 0.001$, $D_E < 0.001$ and $\rho_p = 0.01$). This is predominantly because MMA and C30B are much more compatible than MMA and C93A, which leads to large differences in the structures of the bulk-polymerised samples. This difference in compatibility can be demonstrated in two ways. Firstly, the gel volumes in MMA, which are indicative of monomer–organoclay compatibility, were 91% for C30B and only 67% for C93A. Secondly, the difference in compatibility is evident from theoretical measures of compatibility; ΔHLB is 2.9 for C30B but increases to 8.9 for C93A. Clearly, in terms of the main effects, C30B is better dispersed in MMA and PMMA than C93A.

The interactions for each of the three structural parameters can be seen from a comparison of the slopes of the two lines for each parameter in Fig. 16 (right); large differences in slope, or even a crossover, indicate significant interaction. The C30B and C93A lines for Δd_{001} are virtually parallel, which indicates no interaction for this parameter (P-value of greater than 0.25). The large vertical difference between the parallel lines is simply due to the much greater compatibility of C30B than C93A with MMA; this was discussed in relation to the organoclay main effect. Unlike Δd_{001}, the other two parameters show significant interactions with P-values of 0.001 for D_E and less than 0.001 for ρ_p. The reason for both the interactions becomes apparent after we consider the development of structure in each of the four samples. As established by Dennis et al. [4], the lack of compatibility limits exfoliation during the melt compounding of organoclays that have low compatibility with the molten polymer, even though the shear forces tend to break up the organoclay into tactoids. C93A has a relatively low compatibility with PMMA; consequently, the shear forces applied during the extrusion of C93A tend to breakdown the organoclay agglomerates into tactoids, but further exfoliation of these into single platelets is restricted. In contrast, the far more compatible C30B is amenable to both breakdown of agglomerates into tactoids and subsequent exfoliation of individual layers. The result of this process was that C30B generated a larger D_E value than C93A, but that C93A retained more tactoids, giving a higher ρ_p value than C30B. Considering the bulk-polymerised samples, it was shown above that even untreated MMT can achieve some level of exfoliation; clearly, the absence of modification does not preclude some delamination. The D_E values in Fig. 16 are consistent with this, with C93A reaching approximately 10% exfoliation and C30B approximately 20%; this also fits with the gel volumes measured for these organoclays in MMA. As these values are significantly less than in the extruded samples, large, non-parallel slopes occur in Fig. 16 (right), so that D_E has a significant interaction term. Evidently, the microscale structure in the bulk-polymerised samples is even more sensitive to the effects of chemical compatibility. In fact, though the ρ_p values for the two C30B samples (bulk polymerised and extruded) do not differ greatly, there is an extreme difference in ρ_p between the two C93A samples, which results in the highly significant interaction term for ρ_p. This large difference in

microscale dispersion of C30B and C93A is consistent with work by Ho et al. [103,111] that demonstrated the sensitivity of organoclay structure in organic solvents to compatibility with the solvents. Specifically, it was found that even relatively small changes in chemical compatibility, as measured by solubility parameters, could significantly alter the mean number of layers per tactoid and their aggregation in suspension.

5. Conclusions

In this work, we have applied image analysis to a range of PMMA–clay nanocomposites and have demonstrated that these methods can be used to obtain useful information on the microstructure as well as the more commonly explored nanostructure of such composites. The optimal parameters to quantify microstructure and nanostructure based on the qualification of TEM images are the particle density, ρ_p, and the degree of exfoliation, D_E. While WAXD provides useful insights into structuring of layers within many nanocomposites, it is open to misinterpretation if used as the sole measure of nanocomposite morphology. Therefore, it is essential to complement such data with the more detailed and less easily misconstrued images provided by TEM, particularly when the information contained within the images is quantified by means of image analysis.

From the analysis of the PMMA–clay nanocomposites in this work, we can draw the following additional conclusions.

(1) Simple, quaternary-alkyl ammonium surface modification of MMT dramatically improves polymer intercalation and the dispersion of clay at the microscale in bulk-polymerised PMMA; it has much less impact on exfoliation.
(2) Within the range of 12–16 carbons, alkyl tail length has little effect on the structure in bulk-polymerised PMMA.
(3) A significant reduction in platelet size for otherwise-similar organoclays leads to large increases in exfoliation and the number of particles at the microscale during bulk polymerisation, but has limited effect on polymer intercalation as this depends largely on chemical compatibility.
(4) The incorporation of a polymerisable modifier in an organoclay significantly increases exfoliation and polymer intercalation during polymerisation of PMMA. However, because growth of the polymer chains is a truly nanoscale effect, this has little effect on the microstructure of the PMMA samples.
(5) The presence of excess modifier in the organoclays, especially in large amounts, improves the nanoscale and microscale structures of bulk-polymerised PMMA nanocomposites. However, we question how effective this approach would be for improving the structure, given its cost and the likely undesirable effects on mechanical properties.
(6) In general, extrusion of PMMA nanocomposites produces better structures than bulk polymerisation; structural development is also better for organoclay containing modifiers with single alkyl tails rather than twin alkyl tails.

Acknowledgements

We thank Unimin Australia for the kind donation of the Trubond bentonite sample and Jim Chambers & Associates for the generous provision of the Cloisite samples. The staff and students of the KCPC and the NANO-MNRF at the ACKMM are acknowledged for valuable discussions and training. Thanks also are due to Ms. Kathryn Topp for the HPLC measurements; Dr. Franck d'Agosto for assistance with the ^{1}H NMR spectroscopy measurements on the reactive surfactants; Dr. Garry Warrender for advice on the bulk polymerisation of MMA; and Ms. Anne Simpson for carbon coating the TEM sections. The authors are grateful to Dr. Will P. Gates for many valuable discussions about intercalation/cation exchange chemistry of clays and for indicating the importance of organoclay washing techniques on organic salt content. K.R.R. thanks the University of Sydney for the financial support of this work.

Appendix of symbols

A_f Total field area in high-magnification micrographs for a sample (μm^2)
A_p Particle area (μm^2)
d_{001} Basal spacing of clay layers (nm)
d_{001}^T Basal spacing of clay layers as determined from transmission electron micrographs of nanocomposites (nm)
d_{001}^X Basal spacing of clay layers as determined by X-ray diffraction (nm)
D_E Degree of exfoliation (%): $100(\rho_s/\rho_t\overline{n})$
d_{NN} Next neighbour distance (μm): the distance from the centroid of a particle to the centroid of the closest adjacent particle
d_p Particle diameter (μm)
F_A Agglomeration factor (μm^{-2}): $\rho_t\overline{n} - \rho_s$
F_E Exfoliation factor (μm^{-2}): $(1/M)\sum_{n=1}^{j}((1/n)(N_n/A_f))$
F_S Particle shape factor: the area of the particle divided by the area of a circle of the same perimeter distance as the particle
HLB_D Davies' hydrophile–lipophile balance (HLB) of the surface modifiers
HLB_O Optimal (or required) hydrophile–lipophile balance (HLB) of the MMA–clay system
i Number of particles
j Largest measured number of platelets per particle
M Mass of montmorillonite (MMT) in a sample (wt%)
n Number of platelets per particle ($n = 1, 2, \ldots, j$)
$\overline{n}$ Mean number of platelets per particle
N_F Number of particles in a field
N_n Number of particles in the field area, A_f, that contain n platelets per particle
N_T Total number of particles in the field area, A_f
P_k kth percentile of a distribution, where k is a number between 0 and 100
P_n Total number of platelets in the field area, A_f, in particles that each contain n platelets, such that $N_n = P_n/n$

r^2 "Correlation coefficient" (or the coefficient of determination): the square of the Pearson correlation coefficient, r

r_a Aspect ratio: the maximum ratio of height to width of a bounding rectangle for a particle

r_{NND} Next neighbour distance ratio: the mean d_{NN} in a field divided by the mean d_{NN} for a random array of N_F particles in the field

s Standard deviation

SE_n Standard error in n : $s/\sqrt{N_T}$

α Probability of a "type I error" during hypothesis testing; *i.e.*, of rejecting the null hypothesis when it is true

Δd_{001} Difference between the basal spacing of an organoclay in a nanocomposite and the basal spacing of the original organoclay (nm)

ΔHLB Absolute difference between HLB_D and HLB_O

ϕ_A Area fraction (%): the area of particles in a field relative to the entire area of the field

ρ_p Particle density (μm^{-2}): the number of particles in a field divided by the area of the field

ρ_s Single platelet density (μm^{-2}): $(N_1/A_f)(1/M)$, where N_1 is the total number of single platelets in the field area, A_f

ρ_t Tactoid density (μm^{-2}): $(N_T/A_f)(1/M)$

References

[1] Fu X, Qutubuddin S. Polymer 2001;42(2):807–13.
[2] Lan T, Kaviratna PD, Pinnavaia TJ. Chem Mater 1995;7(11):2144–50.
[3] Zeng CC, Lee LJ. Macromolecules 2001;34(12):4098–103.
[4] Dennis HR, Hunter DL, Chang D, Kim S, White JL, Cho JW, et al. Polymer 2001;42(23):9513–22.
[5] Fornes TD, Yoon PJ, Keskkula H, Paul DR. Polymer 2001;42(25): 9929–40.
[6] Hoffmann B, Dietrich C, Thomann R, Friedrich C, Mulhaupt R. Macromol Rapid Commun 2000;21(1):57–61.
[7] Choi YS, Choi MH, Wang KH, Kim SO, Kim YK, Chung IJ. Macromolecules 2001;34:8978–85.
[8] Huang XY, Brittain WJ. Macromolecules 2001;34(10):3255–60.
[9] Sur GS, Sun HL, Lyu SG, Mark JE. Polymer 2001;42(24):9783–9.
[10] Tseng CR, Wu JY, Lee HY, Chang FC. Polymer 2001;42(25): 10063–70.
[11] Vaia RA, Giannelis EP. Macromolecules 1997;30(25):8000–9.
[12] Vaia RA, Vasudevan S, Krawiec W, Scanlon LG, Giannelis EP. Adv Mater 1995;7(2):154–6.
[13] Wang D, Zhu J, Yao Q, Wilkie CA. Chem Mater 2002;14:3837–43.
[14] Fornes TD, Paul DR. Polymer 2003;44(17):4993–5013.
[15] Kojima Y, Usuki A, Kawasumi M, Okada A, Kurauchi T, Kamigaito O. J Polym Sci Part A Polym Chem 1993;31(4):983–6.
[16] Lan T, Pinnavaia TJ. Chem Mater 1994;6(12):2216–9.
[17] Okada A, Usuki A. Mater Sci Eng C Biomimetic Mater Sens Syst 1995; 3(2):109–15.
[18] Sheng N, Boyce MC, Parks DM, Rutledge GC, Abes JI, Cohen RE. Polymer 2004;45(2):487–506.
[19] Shi H, Lan T, Pinnavaia TJ. Chem Mater 1996;8(8):1584–7.
[20] Alexandre M, Dubois P. Mater Sci Eng R Rep 2000;28(1–2):1–63.
[21] Ray SS, Okamoto M. Prog Polym Sci 2003;28(11):1539–641.
[22] Vaia RA, Liu W. J Polym Sci Part B Polym Phys 2002;40(15): 1590–600.
[23] Vaia RA. Structural characterisation of polymer–layered silicate nanocomposites. In: Pinnavaia TJ, Beall GW, editors. Polymer–clay nanocomposites. Chichester: John Wiley & Sons, Ltd; 2000. p. 229–66.
[24] Manias E, Chen H, Krishnamoorti R, Genzer J, Kramer EJ, Giannelis EP. Macromolecules 2000;33(21):7955–66.
[25] Chin IJ, Thurn-Albrecht T, Kim HC, Russell TP, Wang J. Polymer 2001; 42(13):5947–52.
[26] Lincoln DM, Vaia RA, Wang ZG, Hsiao BS. Polymer 2001;42(4): 1621–31.
[27] Beyer FL, Beck Tan NC, Dasgupta A, Galvin ME. Chem Mater 2002; 14:2983–8.
[28] Morgan AB, Gilman JW. J Appl Polym Sci 2003;87(8):1329–38.
[29] Tabtiang A, Lumlong S, Venables RA. Eur Polym J 2000;36(12): 2559–68.
[30] Vaia RA, Jandt KD, Kramer EJ, Giannelis EP. Chem Mater 1996;8(11): 2628–35.
[31] Kornmann X, Lindberg H, Berglund LA. Polymer 2001;42(10):4493–9.
[32] Ranade A, D'Souza NA, Gnade B. Polymer 2002;43(13):3759–66.
[33] Nam PH, Maiti P, Okamoto M, Kotaka T, Hasegawa N, Usuki A. Polymer 2001;42(23):9633–40.
[34] Marchant D, Jayaraman K. Ind Eng Chem Res 2002;41(25):6402–8.
[35] Fu XA, Qutubuddin S. J Colloid Interface Sci 2005;283(2):373–9.
[36] Chavarria F, Paul DR. Polymer 2004;45(25):8501–15.
[37] Vermogen A, Masenelli-Varlot K, Seguela R, Duchet-Rumeau J, Boucard S, Prele P. Macromolecules 2005;38(23):9661–9.
[38] See Ref. [3].
[39] Yoon PJ, Hunter DL, Paul DR. Polymer 2003;44(18):5341–54.
[40] Grim RE. In: Clay mineralogy. 2nd ed. New York: McGraw-Hill Book Company; 1968.
[41] Nemecz E. In: Clay minerals. Budapest: Akademiai Kiado; 1981.
[42] Gates WP, Anderson JS, Raven MD, Churchman GJ. Appl Clay Sci 2002;20(4–5):189–97.
[43] Yoon PJ, Hunter DL, Paul DR. Polymer 2003;44(18):5323–39.
[44] Meier LP, Kahr G. Clays Clay Miner 1999;47(3):386–8.
[45] Stevens JJ, Anderson SJ. Clays Clay Miner 1996;44(1):132–41.
[46] Bujdak J, Janek M, Madejova J, Komadel P. J Chem Soc Faraday Trans 1998;94(23):3487–92.
[47] Laird DA. Clays Clay Miner 1999;47(5):630–6.
[48] Olis AC, Malla PB, Douglas LA. Clay Miner 1990;25(1):39–50.
[49] Lee SY, Kim SJ. Clays Clay Miner 2002;50(4):435–45.
[50] Lee SY, Kim SJ. Colloids Surf A Physicochem Eng Asp 2002;211(1): 19–26.
[51] Fornes TD, Yoon PJ, Hunter DL, Keskkula H, Paul DR. Polymer 2002; 43(22):5915–33.
[52] Shah RK, Hunter DL, Paul DR. Polymer 2005;46(8):2646–62.
[53] Fornes TD, Hunter DL, Paul DR. Macromolecules 2004;37(5): 1793–8.
[54] Fornes TD, Yoon PJ, Keskkula H, Paul DR. Polymer 2002;43(7): 2121–2.
[55] Janeba D, Capkova P, Weiss Z, Schenk H. Clays Clay Miner 1998; 46(1):63–8.
[56] Matulis CE, Taylor JC. Powder Diffr 1992;7(2):89–94.
[57] Stanjek H, Friedrich R. Clay Miner 1986;21(2):183–90.
[58] Lagaly G, Weiss A. Determination of the layer charge in mica-type layer silicates. In: Heller L, editor. Proceedings of the international clay conference, 1969. Tokyo: Israel Universities Press; 1969. p. 61–80.
[59] Lagaly G, Weiss A. The layer charge of smectitic layer silicates. In: Proceedings of the international clay conference, 1975. Mexico: Applied Publishing Ltd; 1975. p. 157–72.
[60] Lagaly G, Fernandez Gonzalez M, Weiss A. Clay Miner 1976;11(3): 173–87.
[61] Lagaly G. Clay Miner 1981;16(1):1–21.
[62] Stul MS, Uytterhoeven JB. J Colloid Interface Sci 1983;91(1):286–8.
[63] Ratinac KR, Zhu HY, Stadtmueller LM, Ringer SP. Mater Forum 2002; 26(1):44–73.
[64] Ho OB. The determination of Davies HLB increments for cationic surfactants from zeta potential measurements on emulsions. In: Fourth world surfactants congress, Barcelona; 1996. p. 451–61.
[65] Ho OB. J Colloid Interface Sci 1998;198(2):249–60.
[66] Slade PG, Gates WP. Appl Clay Sci 2004;25(1–2):93–101.

[67] Okamoto M, Morita S, Taguchi H, Kim YH, Kotaka T, Tateyama H. Polymer 2000;41(10):3887–90.
[68] Jordan JW. J Phys Colloid Chem 1949;53(2):294–306.
[69] Chen C, Tolle TB. J Polym Sci Part B Polym Phys 2004;42(21): 3981–6.
[70] Yaron-Marcovich D, Chen Y, Nir S, Prost R. Environ Sci Technol 2005; 39(5):1231–8.
[71] Fornes TD, Hunter DL, Paul DR. Polymer 2004;45(7):2321–31.
[72] Young IT. J Histochem Cytochem 1977;25(7):935–41.
[73] Smirnov N. Ann Math Stat 1948;19(2):279–81.
[74] Fornes TD, Paul DR. Macromolecules 2004;37(20):7698–709.
[75] Russ JC. Practical stereology. New York: Plenum Press; 1986.
[76] Underwood EE. Quantitative stereology. Reading, MA: Addison-Wesley Publishing Company Inc; 1970.
[77] Blumstein A. J Polym Sci Part A 1965;3(7):2653–64.
[78] Blumstein A, Blumstein R, Vanderspurt TH. J Colloid Interface Sci 1969;31(2):236–47.
[79] Blumstein A, Parikh KK, Malhotra SL, Blumstein R. J Polym Sci Polym Phys Ed 1971;9(9):1681–91.
[80] Stadtmueller LM, Ratinac KR, Ringer SP. Polymer 2005;46(23): 9574–84.
[81] Okamoto M, Morita S, Kim YH, Kotaka T, Tateyama H. Polymer 2001; 42(3):1201–6.
[82] Jaynes WF, Boyd SA. Soil Sci Soc Am J 1991;55(1):43–8.
[83] Reichert P, Nitz H, Klinke S, Brandsch R, Thomann R, Mulhaupt R. Macromol Mater Eng 2000;275(2):8–17.
[84] Yano K, Usuki A, Okada A. J Polym Sci Polym Chem 1997;35(11): 2289–94.
[85] Utracki LA, Simha R. Polym Int 2004;53(3):279–86.
[86] Kumar S, Jog JP, Natarajan U. J Appl Polym Sci 2003;89(5):1186–94.
[87] Broughton G, Squires L. J Phys Chem 1936;40(8):1041–53.
[88] Hauser EA, Reed CE. J Phys Chem 1937;41(7):911–34.
[89] Messersmith PB, Giannelis EP. Chem Mater 1994;6(10):1719–25.
[90] Cowan CT, White D. Trans Faraday Soc 1958;54(1):691–7.
[91] Weiss A. Angew Chem Int Ed 1963;2(3):135–44.
[92] Slabaugh WH, Kennedy GH. J Colloid Sci 1963;18(4):337–42.
[93] Walker GF. Clay Miner 1967;7(2):129–43.
[94] Slabaugh WH, Hiltner PA. J Phys Chem 1968;72(12):4295–8.
[95] Slabaugh WH, Carter LS. J Colloid Interface Sci 1968;27(2):235–8.
[96] Stul MS, Maes A, Uytterhoeven JB. Clays Clay Miner 1978;26(5): 309–17.
[97] Mortland MM, Shaobai S, Boyd SA. Clays Clay Miner 1986;34(5): 581–5.
[98] Raussell-Colom JA, Serratosa JM. Reactions of clays with organic substances. In: Newman ACD, editor. Chemistry of clays and clay minerals. Essex: Longman Scientific & Technical; 1987. p. 371–422.
[99] Boyd SA, Mortland MM, Chiou CT. Soil Sci Soc Am J 1988;52(3): 652–7.
[100] Favre H, Lagaly G. Clay Miner 1991;26(1):19–32.
[101] Ogawa M, Aono T, Kuroda K, Kato C. Langmuir 1993;9(6):1529–33.
[102] Vaia RA, Teukolsky RK, Giannelis EP. Chem Mater 1994;6(7): 1017–22.
[103] Ho DL, Briber RM, Glinka CJ. Chem Mater 2001;13(5):1923–31.
[104] Bonczek JL, Harris WG, Nkedi-Kizza P. Clays Clay Miner 2002;50(1): 11–7.
[105] Xu SH, Boyd SA. Langmuir 1995;11(7):2508–14.
[106] Boyd SA, Shaobai S, Lee JF, Mortland MM. Clays Clay Miner 1988; 36(2):125–30.
[107] Mandalia T, Bergaya F. J Phys Chem Solids 2006;67(4):836–45.
[108] He H, Duchet J, Galy J, Gerard J-F. J Colloid Interface Sci 2006;295(1): 202–8.
[109] Sobisch T, Lerche D. Colloid Polym Sci 2000;278(4):369–74.
[110] Moraru VN. Appl Clay Sci 2001;19(1–6):11–26.
[111] Ho DL, Glinka CJ. Chem Mater 2003;15(6):1309–12.
[112] Garcia-Lopez D, Gobernado-Mitre I, Fernandez JF, Merino JC, Pastor JM. Polymer 2005;46(8):2758–65.
[113] Morgan AB, Harris JD. Polymer 2003;44(8):2313–20.
[114] Panek G, Schleidt S, Mao Q, Wolkenhauer M, Spiess HW, Jeschke G. Macromolecules 2006;39(6):2191–200.
[115] Xi Y, Ding Z, He H, Frost RL. J Colloid Interface Sci 2004;277(1): 116–20.
[116] Lee SS, Lee CS, Kim MH, Kwak SY, Park M, Lim S, et al. J Polym Sci Part B Polym Phys 2001;39(20):2430–5.
[117] Balazs AC, Ginzburg VV, Lyatskaya Y, Singh C, Zhulina E. Modelling the phase behaviour of polymer–clay nanocomposites. In: Pinnavaia TJ, Beall GW, editors. Polymer–clay nanocomposites. Chichester: John Wiley & Sons, Ltd; 2000. p. 281–313.
[118] Ginzburg VV, Balazs AC. Macromolecules 1999;32(17):5681–8.